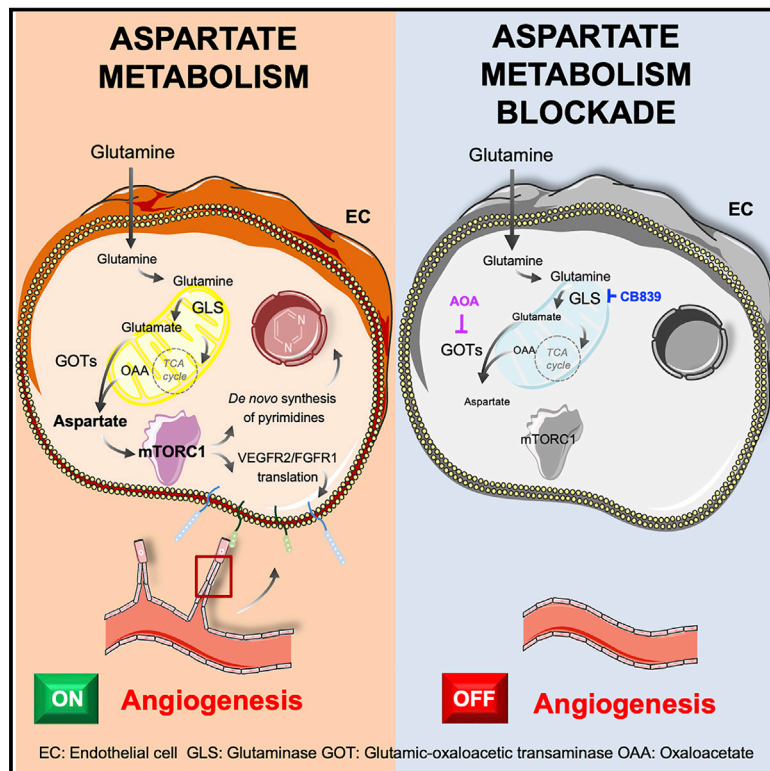# Aspartate metabolism in endothelial cells activates the mTORC1 pathway to initiate translation during angiogenesis

Graphical abstract

ASPARTATE METABOLISM

ASPARTATE METABOLISM BLOCKADE

EC: Endothelial cell GLS: Glutaminase GOT: Glutamic-oxaloacetic transaminase OAA: Oxaloacetate

Authors

Roxana E. Oberkersch,
Giovanna Pontarin, Matteo Astone, ...,
Stefano Biffo, Saverio Tardito,
Massimo M. Santoro

Correspondence

massimo.santoro@unipd.it

In brief

Oberkersch et al. demonstrate that endothelial cells (ECs) use glutamate and transaminase-mediated aspartate to drive angiogenesis in developmental and pathological angiogenesis. Mechanistically, aspartate drives mTORC1 activation that leads to the initiation of translation of endothelial growth factor receptors as well as pyrimidine synthesis in ECs.

Highlights

- Endothelial glutaminolysis is required during tumor and ischemic angiogenesis

- TAs couple glutaminolysis-derived Glu to Asp synthesis in ECs

- mTORC1 activation is driven by Glu and Asp metabolism in ECs

- mTORC1 activation leads to control of endothelial growth factor receptor translation

CellPress

Article

Aspartate metabolism in endothelial cells activates the mTORC1 pathway to initiate translation during angiogenesis

Roxana E. Oberkersch,[1] Giovanna Pontarin,[1] Matteo Astone,[1] Marianna Spizzotin,[1] Liaisan Arslanbaeva,[1] Giovanni Tosi,[1] Emiliano Panieri,[2] Sara Ricciardi,[3] Maria Francesca Allega,[4,5] Alessia Brossa,[2] Paolo Grumati,[6] Benedetta Bussolati,[2] Stefano Biffo,[3] Saverio Tardito,[4,5] and Massimo M. Santoro[1,7,*]

[1]Laboratory of Angiogenesis and Redox Metabolism, Department of Biology, University of Padua, Padua, Italy
[2]Molecular Biotechnology Center, University of Turin, Turin, Italy
[3]National Institute of Molecular Genetics (INGM) and Department of Biosciences, University of Milan, Milan, Italy
[4]Cancer Research UK Beatson Institute, Garscube Estate, Switchback Road, Glasgow G611BD, UK
[5]Institute of Cancer Sciences, University of Glasgow, Garscube Estate, Switchback Road, Glasgow G611QH, UK
[6]Telethon Institute of Genetics and Medicine (TIGEM), Pozzuoli, Italy
[7]Lead contact
*Correspondence: massimo.santoro@unipd.it
https://doi.org/10.1016/j.devcel.2022.04.018

SUMMARY

Angiogenesis, the active formation of new blood vessels from pre-existing ones, is a complex and demanding biological process that plays an important role in physiological as well as pathological settings. Recent evidence supports cell metabolism as a critical regulator of angiogenesis. However, whether and how cell metabolism regulates endothelial growth factor receptor levels and nucleotide synthesis remains elusive. We here shown in both human cell lines and mouse models that during developmental and pathological angiogenesis, endothelial cells (ECs) use glutaminolysis-derived glutamate to produce aspartate (Asp) via aspartate aminotransferase (AST/GOT). Asp leads to mTORC1 activation which, in turn, regulates endothelial translation machinery for VEGFR2 and FGFR1 synthesis. Asp-dependent mTORC1 pathway activation also regulates *de novo* pyrimidine synthesis in angiogenic ECs. These findings identify glutaminolysis-derived Asp as a regulator of mTORC1-dependent endothelial translation and pyrimidine synthesis. Our studies may help overcome anti-VEGF therapy resistance by targeting endothelial growth factor receptor translation.

INTRODUCTION

Angiogenesis, the formation of new blood vessels, is a complex and demanding biological process that plays an important role in physiological as well as pathological conditions such as cancer and ischemia (Apte et al., 2019; Potente and Makinen, 2017). Emerging evidence reveals that endothelial cell (EC) metabolism controls physiological angiogenesis and that ECs rely on specific metabolic pathways (Diebold et al., 2019; Li et al., 2019; Longchamp et al., 2018). However, how these pathways are used to support angiogenesis and EC signaling is still far from being completely understood.

Extracellular nutrients and growth factors together regulate EC growth, quiescence, and survival during angiogenesis. Although it is well described that endothelial growth factor pathways (e.g., VEGFRs and FGFR1) may initiate anabolic metabolism, leading, for example, to glucose import (Yu et al., 2017) and fatty acid uptake (Hagberg et al., 2010), whether and how nutrients regulate growth factor receptors and signaling are poorly understood. The mTOR pathway senses and integrates signals from growth factors and from the metabolic states of the cells to support cell growth. mTORC1/2 signaling is frequently activated in tumors, controlling cancer cell metabolism by regulating several metabolic enzymes and growth factor responses (Ben-Sahra and Manning, 2017; Mossmann et al., 2018; Saxton and Sabatini, 2017). Interestingly, mTORC2 signaling has been shown to be relevant in VEGF signaling during angiogenesis (Karali et al., 2014). However, a functional understanding of how mTORC1 signaling coordinates metabolism and growth factor response is still missing in ECs during angiogenesis.

By using genetic, metabolic, and proteomic approaches, we discover that ECs use glutaminolysis-derived glutamate (Glu) and aspartate (Asp) to support retinal vascular growth and promote tumor and ischemic angiogenesis. Asp aminotransferase (AST/GOT) is used by ECs to produce Asp that in turn controls the translation of endothelial growth factor receptors and pyrimidine synthesis via the activation of the mTORC1 signaling pathway. We anticipate our study to be a starting point for novel therapeutical anti-angiogenic approaches based on the inhibition of glutaminase (GLS) and GOT enzymes to target endothelial growth factor receptor translation machinery and nucleotide synthesis in disease settings.
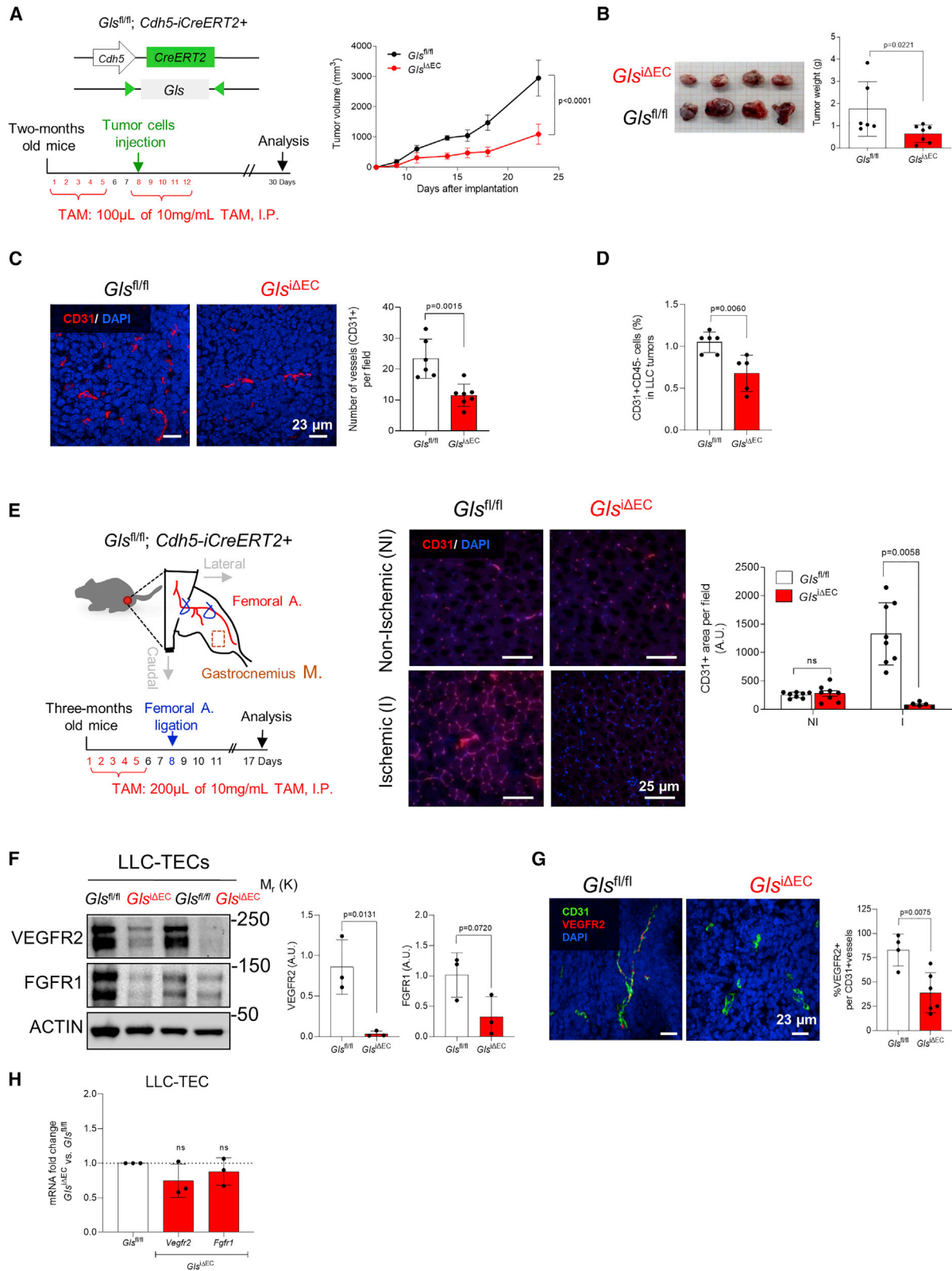
RESULTS

Glutamate (Glu) is required for pathological angiogenesis

ECs use a large amount of glutamine (Gln) to synthesize Glu through GLS, a metabolic process called glutaminolysis (Huang et al., 2017; Kim et al., 2017). We used animal models bearing conditional alleles of the glutaminolytic enzyme, GLS, to investigate whether Glu synthesis via GLS plays an important role during pathological angiogenesis *in vivo*. We then generated mice lacking *Gls* in ECs (*Gls*[iΔEC]) using mice bearing a conditional floxed allele of *Gls* (Mingote et al., 2015) intercrossed with *Cdh5*-CreERT2 or *Pdgfb*-CreERT2 mice (EC-specific tamoxifen [TAM]-inducible Cre-driven lines). At first, we subcutaneously implanted Lewis lung carcinoma (LLC) cells in *Gls*[iΔEC] mice, and we observed a significant reduction of tumor growth, evaluated as tumor volume and weight (Figures 1A and 1B). The efficiency of GLS knockdown (KD) in LLC-derived tumor ECs (LLC-TECs) and neonatal micropulmonary ECs (MPECs) was confirmed at DNA, mRNA, and protein levels (Figures S1A–S1C). LLC tumors derived from *Gls*[iΔEC] mice exhibited a significantly reduced number of vessels (Figure 1C) and CD31^{+}/CD45^{−} cells (Figure 1D). We determined that the lack of vessels led to an impairment of cell proliferation in the *Gls*[iΔEC] tumor mass and an increase in cell death (Figures S1D and S1E). The rare tumor vessels of *Gls*[iΔEC] mice exhibited less coverage by vascular smooth muscle cells (Figure S1F). We also performed tumor transplantation experiments using B16F10 melanoma cells with analogous results (Figures S2A and S2B). B16F10 tumors derived from *Gls*[iΔEC] mice showed a reduced number of vessels (Figure S2C). These results imply that endothelial GLS is required during VEGF-mediated tumor growth *in vivo*.

Next, we investigated whether GLS is involved in postnatal angiogenesis in a mouse model of hindlimb ischemia (Limbourg et al., 2009). *Gls*[iΔEC] and control (CTRL) mice were subjected to surgical ligation of the femoral artery, a procedure that triggers neovascularization of the ischemic tissue with the formation of new blood vessels. Ischemic angiogenesis was scored in the CTRL mice but not in *Gls*[iΔEC] mice (Figure 1E). These data show that *Gls*[iΔEC] mice are not able to respond to neovascularization signals driven by ischemic tissues (Arsic et al., 2004).

To understand how glutaminolysis regulates pathological angiogenesis, we characterized LLC-TECs from *Gls*[iΔEC] mice (Figure 1F). *Gls*[iΔEC] tumor ECs exhibited lower levels of VEGFR2 than CTRL cells. Also, FGFR1, another critical endothelial growth factor receptor, was significantly reduced in *Gls*[iΔEC] TECs compared with CTRLs. By using immunofluorescence staining we confirmed that CD31^{+} tumor vessels derived from *Gls*[iΔEC] mice showed reduced VEGFR2 expression (Figure 1G). We found that the decrease of VEGFR2 and FGFR1 proteins was not caused by changes in VEGFR2 or FGFR1 mRNA levels, since mRNAs of both receptors were comparable between *Gls*[iΔEC] and CTRL mice (Figure 1H). Similarly, TECs isolated from B16F10 tumors in *Gls*[iΔEC] mice also showed a distinct decrease of VEGFR2 and FGFR1 protein levels, but not of another endothelial receptor such as VEGFR1 (Figure S2D). Taken together, these findings reveal a critical function for glutaminolysis and Glu synthesis during *in vivo* tumor and ischemic angiogenesis by controlling the levels of endothelial growth factor receptors in a transcriptional-independent manner.

GLS-derived Glu regulates VEGFR2 levels and pyrimidine biosynthesis

To further investigate how glutaminolysis affects endothelial growth factor receptor synthesis and angiogenesis, we treated human umbilical vein ECs with the GLS inhibitor (CB839) and with shRNA against GLS (GLS[KD]). As a positive CTRL we also cultured them in the absence of Gln. Both pharmacological and genetic GLS blockade significantly reduced the levels of Glu compared with the CTRLs in ECs as evaluated by high-performance liquid chromatography mass spectrometry (HPLC-MS) analyses (Figure 2A). In parallel, we confirmed the silencing and mitochondrial localization of GLS in ECs in our experimental conditions (Figures S3A–S3C; Altman et al., 2016). We then measured protein levels of endothelial growth factor receptors such as VEGFR1, VEGFR2, and FGFR1 (Figures 2B, S3D, and S3E). Although the level of VEGFR1 was unchanged

---

Figure 1. EC-loss of Glu synthesis by *Gls* KO impairs pathological angiogenesis *in vivo*

(A) Outline of tumor angiogenesis experiments using endothelial inducible *Gls* KO animals (*Gls*[iΔEC]). After tamoxifen (TAM) administration, Lewis Lung carcinoma (LLC) cells were inoculated subcutaneously into *Gls*^{fl/fl} and *Gls*[iΔEC] 2-month-old mice. Tumor volumes were scored 24 days after tumor inoculation. Data are shown as mean ± SD of n ≥ 6 mice per group; statistical comparison is from two-way ANOVA test.

(B) Tumors were collected and weighed at the endpoint of the experiment in (A). Data are shown as mean ± SD of n ≥ 6 mice per group. p value is determined by two-tailed Student's t test.

(C) Representative images of LLC tumor vasculature (left) stained with CD31 (red, labeling EC) and DAPI (blue, labeling nuclei) and their quantification (right). Data are shown as mean ± SD of n ≥ 6 mice per group; p value is determined by two-tailed Student's t test.

(D) Quantification of CD31^{+}CD45^{−} cells of *Gls*^{fl/fl} and *Gls*[iΔEC] LLC tumors at the end point of (A) by cytometric analysis. Data are shown as mean ± SD of n ≥ 5 mice per group; p value is determined by two-tailed Student's t test.

(E) Schema of hindlimb ischemia mouse model. Representative immunofluorescence images of gastrocnemius muscle in *Gls*^{fl/fl} and *Gls*[iΔEC] mice after 10 days of femoral artery ligation (ischemic, I) or not (non-ischemic, NI) stained for CD31 (red) and DAPI (blue). Data are shown as mean ± SD of n ≥ 6 mice per group; p value is determined by two-tailed Student's t test.

(F) Immunoblot analysis of VEGFR2 and FGFR1 of *Gls*^{fl/fl} and *Gls*[iΔEC] LLC tumor endothelial cells (LLC-TECs) isolated by magnetic cell sorting system (Miltenyi Biotec). Quantification of bands was performed using ImageJ software and normalized against ACTIN. Data are shown as mean ± SD of n = 3 mice per group; p values are determined by two-tailed Student's t test.

(G) Immunofluorescence of *Gls*^{fl/fl} and *Gls*[iΔEC] LLC tumors stained for VEGFR2 (red), CD31 (green), and DAPI (blue) (left). Percentage of VEGFR2+ vessels (VEGFR2+CD31+ vessels) is quantified (right). Data are shown as mean ± SD of n ≥ 4 mice per group; p value is determined by two-tailed Student's t test.

(H) Transcript levels of *Vegfr2* and *Fgfr1* of *Gls*^{fl/fl} and *Gls*[iΔEC] LLC-TEC. Data are shown as mean ± SD of n = 3 mice per group, p value is determined by one sample t test.
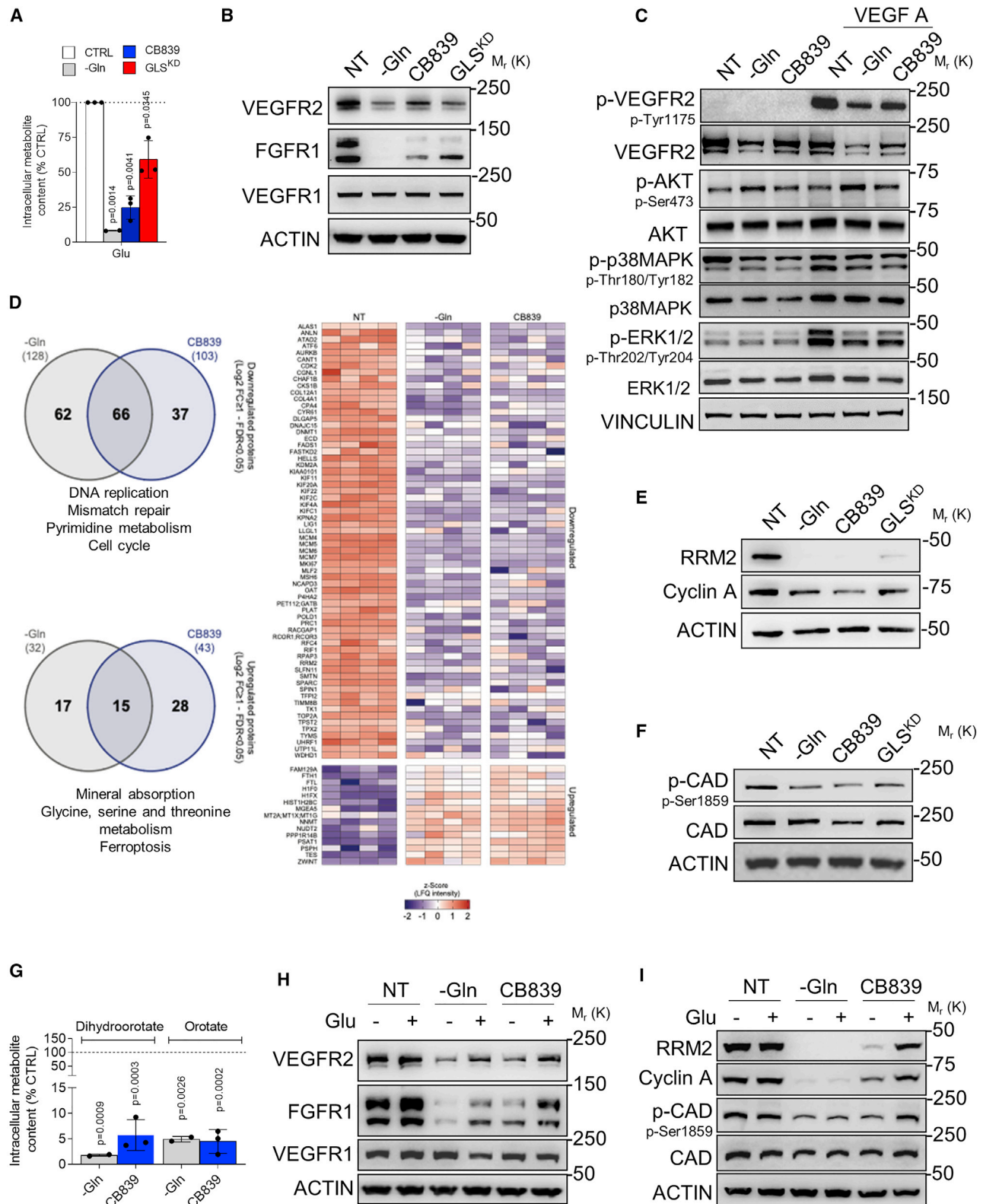
See also Figures S1 and S2.

Figure 2. GLS-derived Glu is crucial for endothelial growth factor receptor protein levels and pyrimidine biosynthesis

(A) Intracellular content of Glu in ECs deprived of Gln (−Gln), treated with 200 nM CB839, and silenced for GLS (GLS[KD]). Data are expressed as % of control (mean ± SD) of three (CB839 and GLS[KD]) or two (−Gln) independent experiments. p values are determined by one sample t test compared with the control.

among all conditions, VEGFR2 and FGFR1 proteins (but not their corresponding mRNAs) were significantly reduced (Figure S3E). The decrease of VEGFR2 protein occurred both in proliferating and unstimulated cells (Figure S3F), leading to a reduced net amount of VEGFR2 protein in the plasma membrane, as shown by biotinylation experiments (Figure S3G). To test whether glutaminolysis blockade might lead to an impairment of VEGF signaling, we stimulated cells with VEGF-A for 15 min upon Gln deprivation and CB839 treatment and analyzed VEGFR2 tyrosine phosphorylation as well as canonical VEGF downstream signaling (Figures 2C and S3H). Except for Akt activation, which remained unchanged (or even increased in Gln-deprived conditions), both treatments impaired ligand-dependent VEGFR2 phosphorylation as well as ERK1/2 and p38MAPK downstream signaling pathways activation. These data indicate that downregulation of VEGFR2 levels induced by Glu deficiency attenuates VEGF-dependent signaling, explaining the impairment of the angiogenic responses in $Gls^{i\Delta EC}$ animals.

Pathological angiogenesis is strictly dependent on the capacity of ECs to escape from quiescent conditions and to re-enter into the cell cycle for cell proliferation. We then investigated EC proliferation in Gln-deprived and glutaminolysis blockade conditions (Figure S3I). We also analyzed the distribution of cells within the different phases of the cell cycle when glutaminolysis is blocked (Figure S3J). Notably, in the absence of Gln in GLS^KD- or CB839-treated cells, we observed a reduction in the cellular proliferation rate and a block in the G0/G1 cell-cycle phase. To understand the mechanism through which glutaminolysis blockade impairs EC proliferation, we performed proteomic analyses on Gln-deprived and CB839-treated cells (Figure 2D; Tables S1 and S2). From a total of 4,020 proteins analyzed, 66 proteins were down-regulated in a common fashion across all treatments compared with the CTRL. KEGG pathways analyses revealed enrichment for mismatch repair (MSH6, RFC4, LIG1, and POLD1), cell cycle (minichromosome maintenance complex component and CDK2), and pyrimidine metabolism (CANT1, RRM2, TK1, and TYMS) signature. On the contrary, 15 proteins were upregulated, which are mainly involved in glycine (Gly), serine (Ser), and threonine (Thr) metabolism (PSPH and PSAT1) and ferroptosis regulation (FTH1 and FTL). To confirm these proteomic data, we analyzed the protein level of cyclin A and ribonu-

cleotide reductase (RNR, a cell-cycle-regulated enzyme that catalyzes the rate-limiting step in the *de novo* synthesis of DNA precursors [Nordlund and Reichard, 2006; Figure 2E]). Both cyclin A and the small subunit R2 of RNR (RRM2) levels dropped in Gln-deprived conditions as well as upon glutaminolysis inhibition, explaining the decrease in cell proliferation. In addition, we also analyzed p27^KIP expression, a marker for cell-cycle inhibition, which again confirmed the proliferation block upon glutaminolysis blockade (Figure S3K).

The marked decrease of RRM2 protein levels seen in Glu-deficient cells prompted us to examine in more detail nucleotide synthesis in ECs. Nucleotides are recycled from existing nucleosides through the salvage pathway or synthesized *de novo* (Chandel, 2021). The nitrogen groups required for the *de novo* nucleotides biosynthesis derive from Gln, Gly, and Asp, while the ribose moiety is derived from the pentose phosphate pathway (PPP) (Tong et al., 2009). Our data showed that the level of glycolytic intermediates and pentose phosphates are not decreased upon Gln starvation or glutaminolysis inhibition, thus excluding that ribose-P limits nucleotide biosynthesis (Figures S4A and S4B). We next assessed the activation of the enzymatic complex involved in the initial steps of the *de novo* pyrimidine biosynthesis (carbamoyl-phosphate synthetase 2, Asp transcarbamoylase, dihydroorotase [CAD]). We observed that both Gln deprivation and GLS inhibition reduced CAD phosphorylation at Ser1859 (Figure 2F). To test whether the reduced CAD phosphorylation affects its enzymatic activity, we measured the intracellular levels of the CAD product: dihydroorotate and orotate (Figure 2G). Strikingly, both Gln deprivation and CB839 treatment markedly reduced the intracellular levels of these two intermediates of the pyrimidine biosynthetic pathway.

We performed rescue experiments by overexpressing VEGFR2 in Gln-deprived and CB839-treated cells and evaluated the extent of proliferation rescue by assessing cell number and expression of both cyclin A and RRM2 markers (Figures S4C and S4D). We confirmed that overexpressed VEGFR2 could be properly activated and phosphorylated by VEGF stimulation (Figure S4E). Although Gln-deprived cells were unaffected by VEGFR2 overexpression, CB839-treated cells were partially rescued in their proliferative capacity, indicating that restored VEGFR2 synthesis can only temporarily rescue the proliferation defects.

(B) Immunoblot analysis of endothelial growth factor receptors: VEGFR2, FGFR1, and VEGFR1 in ECs deprived of Gln (−Gln) or treated with 200 nM of CB839 for 24 h, and GLS^KD (96 hpi).

(C) Immunoblot analysis of VEGFR2 signaling p-VEGFR2 (p-Tyr1175 and total), p-AKT (p-Ser473 and total), p-p38MAPK (p-Thr180/182, and total), and p-ERk1/2 (p-Thr202/204 and total) upon stimulation with 25 nM VEGF A for 15 min in ECs starved for Gln (−Gln) or treated with 200 nM CB839 for 24 h.

(D) Left: Venn diagram of down- and upregulated proteins in −Gln and CB839, respectively, to the control ($\log_2$ fold-change ≥ 1 and FDR ≤ 0.05). KEGG pathways are reported under the Venn diagram. Right: heatmap of label-free quantitation (LFQ) intensities of significantly changed proteins represented in the Venn diagram.

(E) Representative immunoblots of three independent experiments of RRM2, and cyclin A of ECs deprived of Gln (−Gln), treated with 200 nM CB839 or silenced for GLS (GLS^KD).

(F) Representative immunoblots of p-CAD (p-Ser1859) and total protein of three independent experiments of ECs deprived of Gln (−Gln), treated with 200 nM CB839, or silenced for GLS (GLS^KD).

(G) Intracellular content of dihydroorotate and orotate in ECs deprived of Gln (−Gln) or treated with 200 nM CB839. Data are expressed as % of control (mean ± SD) of three (CB839) or two (−Gln) independent experiments. p values are determined by one sample t test.

(H) Rescue experiment of endothelial growth factor receptors: VEGFR2, FGFR1, and VEGFR1 using 2 mM Glu of ECs deprived for Gln or treated with 200 nM CB839 for 24 h.

(I) Representative immunoblots of three independent experiments (n = 3) of RRM2, cyclin A, and CAD (p-Ser1859 and total) of ECs deprived of Gln (−Gln) or treated with 200 nM CB839 in the presence or absence of 2 mM Glu for 24 h.

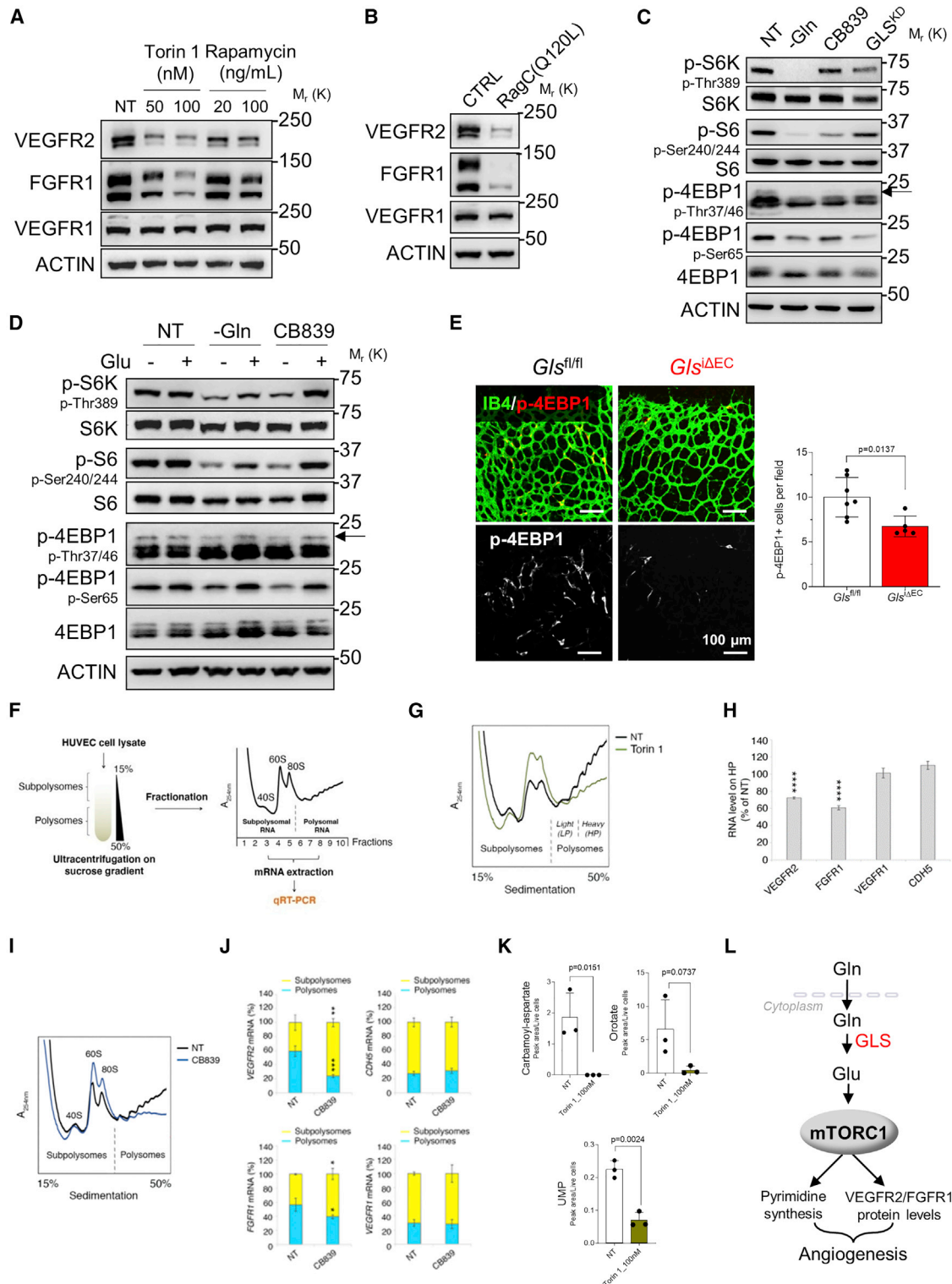See also Figures S3 and S4 and Tables S1 and S2.

Figure 3. Glu-dependent mTORC1 activation specifically regulates translation

(A) Immunoblot analysis of VEGFR2, FGFR1, and VEGFR1 levels in ECs treated with Torin1 (50, and 100 nM) and rapamycin (20 and 100 ng/mL) for 24 h.

(B) Immunoblot analysis of VEGFR2, FGFR1, and VEGFR1 levels in EC-expressing inactive GFP-RagC (Q120L) for 48 h. HUVEC were infected with lentivirus carrying pLVX-TETONE-GFP-RagC-Q120L inducible lentiviral plasmid for 72 h and treated with 2 μg/mL doxycycline for an additional 48 h.

(C) Immunoblot analysis of mTORC1 signaling: S6K (p-Thr389 and total), S6 (p-Ser240/244 and total), and 4EBP1 (p-Thr37/46, p-Ser65 and total) were evaluated in ECs deprived of Gln (−Gln), treated with 200 nM CB839, and silenced for GLS (GLS^KD).

(legend continued on next page)

To test whether Glu levels were limiting VEGFR2 synthesis and proliferation of ECs upon Gln depletion and glutaminolysis inhibition, we supplemented Glu to ECs. Glu supplementation alone was sufficient to partially restore VEGFR2 and FGFR1 protein levels in these conditions (Figures 2H and S4F). In addition, Glu supplementation was able to rescue cell proliferation markers and CAD activation in GLS blockade conditions but not in Gln-restricted conditions (Figure 2I). These data indicate that Glu produced by glutaminolysis supports angiogenesis by regulating the levels of endothelial growth factor receptors such as VEGFR2 and FGFR1 and supports the *de novo* pyrimidine biosynthesis (Figure S4G).

Glu leads to mTORC1-dependent VEGFR2 translation control in EC

Next, we investigated how Glu regulates VEGFR2 protein levels, and we hypothesized that this might occur through increased degradation or reduced translation of the receptor. At first, we decided to test autophagy-dependent protein degradation of VEGFR2 by treating ECs with chloroquine (CQ) or bafilomycin (BA), which are two inhibitors of autophagy (Figure S5A). These compounds alone, or in combination with Gln starvation or CB839 treatment, did not produce an alteration of VEGFR2 levels (Figure S5B). We also tested whether proteasomal-dependent degradation was engaged by using the specific proteasome inhibitor MG132, but this inhibitor did not rescue the VEGFR2 protein levels under Gln deprivation or after CB839 treatment (Figure S5C). Since the mTORC1 pathway regulates protein synthesis, we reasoned that it might represent a functional link between metabolic state and endothelial growth factor receptor levels in ECs (Saxton and Sabatini, 2017). We therefore treated ECs with two mTORC1 inhibitors, rapamycin and Torin1 and evaluated receptor protein levels (Figures 3A and S5D). Rapamycin treatment modestly alters VEGFR2 and FGFR1 protein levels, while Torin1 treatment severely induced their decrease. In both the cases, VEGFR1 levels were unaffected. We show that although both S6 kinase (S6K) and eukaryotic translation initiation factor 4E (eIF4E)-binding protein 1 (4E-BP1) are direct targets of the mTORC1 complex, rapamycin and Torin1 inhibitors differently regulate these branches in ECs (Figure S5E; Choo et al., 2008). Moreover, inducible expression of inactive RagCQ120L that completely blocked mTORC1-dependent

S6K/4EBP1 phosphorylation in response to amino acid stimulation (Kim et al., 2008) impaired VEGFR2 and FGFR1 but not VEGFR1 protein synthesis (Figures 3B, S5F, and S5G). These data suggest a critical role for mTORC1 activity in regulating endothelial growth factor receptor synthesis.

It has been previously proposed that glutaminolysis is required to activate mTORC1 signaling in cancer cell lines (Durán et al., 2012); nevertheless, to different extents, Gln deprivation, CB839 treatment, and GLS^{KD} impaired both S6K and 4EBP1 branch activation (Figures 3C and S5H). Accordingly, we tested whether mTORC1 activation could be rescued by Glu and found that Glu supplementation was sufficient to rescue mTORC1 signaling in Gln-deprived and CB839-treated cells (Figures 3D and S5I). To confirm that mTORC1 activation is also Glu-dependent in pathological settings, murine TECs isolated from LLC and B16F10 tumors from glutaminolysis-impaired mice (Gls^{iΔEC}) were analyzed for mTORC1 signaling (Figures S6A–S6C). mTORC1 activation was found to be inhibited in Gls^{iΔEC} compared with CTRL mice. We conclude that TECs lacking Glu have decreased mTORC1 activity. To prove that the functional link between glutaminolysis and mTORC1 activation also occurs in developmental angiogenesis, we analyzed 4EBP1 activation in a postnatal model of mouse retina. Proliferating ECs at the vascular front of the retina that actively divide show robust 4EBP1 phosphorylation and mTOR activation (Figure 3E). Strikingly, endothelial loss of GLS reduced mTORC1/4EBP1 activation in retinal angiogenic cells, explaining the vascular defects observed in Gls^{iΔEC} mice (Figure S6D). These data indicate that glutaminolysis and Glu synthesis play an important role in the regulation of angiogenesis through mTORC1 signaling.

mTOR signaling is a master regulator of mRNA translation (Ma and Blenis, 2009). To study mTORC1-dependent translation in ECs, we took advantage of polysome profile analyses (Figure 3F) (Panda et al., 2017; Ricciardi et al., 2018). We tested the dependence of VEGFR2, VEGFR1, and FGFR1 endothelial growth factor receptors as well as CDH5 mRNA translation by evaluating the effective amount of their mRNAs on heavy polysomes (HPs) of ECs upon mTORC1 inhibition with Torin1. Our data show that the mTORC1 blockade specifically impairs the translation of VEGFR2 and FGFR1 mRNAs in ECs, as shown by the lower polysomal incorporation of these transcripts in Torin1-treated ECs with respect to CTRL (Figures 3G and 3H). We

---

(D) Rescue experiment of mTORC1 signaling using 2 mM Glu of ECs deprived of Gln (−Gln) or treated with 200 nM CB839.

(E) Confocal analysis of mTORC1 activation (red, p-4EBP1 labeling) in the retinal vasculature (green, isolectin B4 labeling) at postnatal day 6 in Gls$^{fl/fl}$ and Gls^{iΔEC} mice. p value is determined by two-tailed Student's t test.

(F) Schematic protocol for polysome profiling analysis. Cell lysates were sedimented on sucrose gradients to separate polysomes and co-translated mRNAs from subpolysomes and untranslated or poorly translated mRNAs. mRNA was extracted from the polysomal and subpolysomal fraction and analyzed by qRT-PCR. The amount of mRNA associated with the polysomal fraction is an index of its rate of initiation of translation (see also STAR Methods section).

(G) Polysome profiles of ECs treated with 100 nM Torin1 and untreated (NT) for 1 h.

(H) Quantification of mRNA levels in heavy polysome (HP) fractions of the following: VEGFR2, FGFR1, CDH5, and VEGFR1, in ECs treated with 100 nM Torin1 for 1 h or untreated (NT). p values are determined by two-tailed Student's t test.

(I) Polysome profiles of 200 nM CB839 treated and untreated (NT) ECs during 24 h.

(J) Quantification of mRNA levels in subpolysome and polysome fractions of: VEGFR2, FGFR1, CDH5, and VEGFR1, in ECs treated with 200 nM CB839 for 24 h or untreated (NT) for 24 h. p values are determined by two-tailed Student's t test.

(K) Intracellular content of carbamoyl-aspartate, orotate, and UMP in ECs treated with 100 nM Torin1 for 24 h. Data are expressed as peak area/live cells (mean ± SD) of three independent experiments. p values are determined by two-tailed Student's t test compared with the control.

(L) A schematic representation showing endothelial GLS-derived Glu activation of mTORC1 signaling to support endothelial growth factor receptors (VEGFR2 and FGFR1) translation and pyrimidine synthesis.

See also Figures S5 and S6.

next performed a polysomal profile of ECs untreated or treated with CB839 (Figure 3I). Polysome profiles of ECs upon Glu deprivation induced by CB839 treatment showed an increase of 80S peak, with a concomitant decrease of polysomes, which is a clear indication of reduction of translation initiation. We next performed qRT-PCR analysis of the distribution of their mRNAs on polysomal gradient fractions (Figure 3J). We found that glutaminolysis blockade specifically impairs the translation of VEGFR2 and FGFR1 mRNAs, as it leads to a shift of VEGFR2 and FGFR1 mRNAs from active translating polysomes to non-translating subpolysomal fractions. On the contrary, VEGFR1 and CDH5 mRNA translation were unaffected by direct mTORC1 inhibition and glutaminolysis impairment.

It has been shown that mTORC1 and the downstream S6K selectively control the synthesis of pyrimidines through direct CAD phosphorylation and activation (Ben-Sahra et al., 2013; Robitaille et al., 2013). To test whether pyrimidine synthesis is also directly controlled by mTORC1 signaling in ECs, we treated ECs with Torin1 and analyzed the levels of pyrimidine precursors directly controlled by CAD such as carbamoyl-Asp, orotate, and uridine-5′-monophosphate (UMP) (Figure 3K). All these precursors were significantly decreased after mTORC1 inhibition. We conclude that together with VEGFR2/FGFR1 translation control, pyrimidine synthesis is an underlying mechanism by which mTORC1 activation promotes angiogenesis in ECs and, consequently, by which mTORC1 inactivation followed by GLS inhibition reduces EC proliferation and angiogenesis (Figure 3L).

Transaminases regulate Asp metabolism in ECs

mTORC1 activity is controlled by growth factors, amino acids, and stress conditions (Palm and Thompson, 2017; Saxton and Sabatini, 2017). To examine the mechanism through which Glu could affect mTORC1 activity and angiogenesis, we performed a metabolomic analysis to measure metabolic changes upon Gln deprivation and glutaminolysis blockade. We focused on Gln-derived non-essential amino acids (NEAAs), mTORC1-sensing amino acids (mTORC1-AAs), and tricarboxylic acid (TCA) cycle intermediates (Figures S7A and S7B). Surprisingly, although the glutaminolysis blockade did not affect leucine (Leu), arginine (Arg), methionine (Met), and Gln levels (known activators of the mTORC1 pathway), it significantly lowered the Glu, Asp, and Asn levels. Previous data reported that most TCA carbons in ECs are derived from Gln (Kim et al., 2017). Accordingly, the levels of citrate, α-ketoglutarate (α-KG), succinate, and malate dropped significantly upon GLS blockade. It has been shown that α-KG could regulate mTORC1 activation (Durán et al., 2012). Therefore, we next focused on the role of α-KG and Asp/Asn to elucidate the mechanisms underlying the blockade of mTORC1 activation in ECs.

Glu can be converted to α-KG and ammonium (NH_4^+) by Glu dehydrogenases (GLUD1/2) or to α-KG and NEAA by transaminases (TAs) (Figure 4A). In contrast to GLUD, which releases NH_4^+ in generating α-KG, these TAs mediate the reversible transfer of the α-amino nitrogen from Glu to an α-ketoacid, generating the NEAAs Ser, Ala, and Asp. To investigate whether angiogenic ECs use Glu metabolism via GLUD or TAs to activate mTORC1, we treated ECs with R162 (a specific chemical inhibitor of GLUD1/2; Jin et al., 2015) and aminooxyacetic acid (AOA, an inhibitor of pyridoxal phosphate (PLP)-dependent TAs; Thornburg

et al., 2008). Although R162 treatment did not alter VEGFR2 and FGFR1 levels, AOA selectively and significantly reduced them, but not those of VEGFR1 (Figures 4B and S7C). These data resemble the Glu-deficient conditions achieved by GLS inhibition (Figure 2B). We next compared the proteome of AOA-treated cells with the one of CB839-treated cells (Figure S7D; Tables S1 and S2). We observed that AOA or CB839 treatment had a similar proteomic signature, suggesting a common proteomic adaptation under metabolic stress such as Gln deprivation, glutaminolysis, and TAs blockade. Here, 41 proteins were down-regulated in a common fashion across all treatments compared with the CTRL. The down-regulated proteins included RRM2, TK1, involved in pyrimidine synthesis, and MSH6, LIG1, related to mismatch repair. Thus, 21 proteins were upregulated and mainly involved in Ser biosynthesis (PSPH and PSAT1) and ferroptosis regulation (FTH1 and FTL). To confirm these data, we evaluated the effect of R162 and AOA treatment on EC proliferation markers such as RRM2 and cyclin A levels as well as cell number (Figures 4C and S7E). Although the GLUD blockade did not affect EC proliferation, TA inhibition severely impaired the EC proliferation rate compared with CTRL cells. Next, we tested how these inhibitors affect mTORC1 activation (Figures 4D and S7F). The inhibition of TAs but not of GLUD significantly affected S6K and 4EBP1 branches, supporting a role for TA-derived NEAA in mTORC1 activation. Accordingly, we evaluated whether TA-mediated Glu metabolism might influence the translational machinery, and we analyzed the polysomal profiles of ECs upon R162 or AOA treatment (Figure 4E). TAs blockade induced an increase of the 80S peak, together with a sharp decrease of polysomes, an indication of translation initiation blockade. We also analyzed the distribution of VEGFR2 and FGFR1 mRNAs on polysomal gradient fractions of ECs untreated or treated with R162 or AOA (Figure 4F). We found that TA, but not GLUD, inhibition impairs VEGFR2 and FGFR1 translation, as pointed out by the accumulation of the majority of VEGFR2 and FGFR1 mRNAs on non-translating subpolysomes.

To identify which TA is involved in Glu metabolism, we used a metabolic approach. We scored among TA-dependent NEAAs the ones whose levels were consistently affected by CB839 and AOA treatments in ECs (Figure 4G). Asp and P-Serine (P-Ser) were the most affected, with a significant drop in both CB839- and AOA-treated cells. We confirmed these data by using stable isotope tracing techniques (Figure 5A). ECs that were maintained in media containing $^{13}C_5$Gln and treated with CB839 and AOA revealed lower levels of Gln-derived Glu, α-KG, Asp, Asn, and TCA cycle intermediates (Figure 5B). Moreover, CB839 and AOA treatments impaired pyrimidine biosynthesis, as indicated by the smaller fraction of carbamoyl-Asp, orotate, uridine 5′-triphosphate (UTP), and cytidine-5'-triphosphate (CTP), incorporating Gln-derived ^{13}C atoms (Figure 5C) and supporting the contributions of GLS and TAs to pyrimidine intermediates biosynthesis.

We then addressed the impact of α-KG and Asp supplementation on mTORC1 activity upon TAs inhibition with AOA. Asp supplementation alone, but not α-KG alone, significantly restored VEGFR2 and FGFR1 levels (Figures 6A and S8A). Accordingly, we concluded that Asp, but not α-KG, supplementation is able to fully rescue mTORC1 signaling when inhibited by AOA treatment (Figures 6B and S8B). These data fit with the metabolic analyses of NEAA and TCA intermediates in
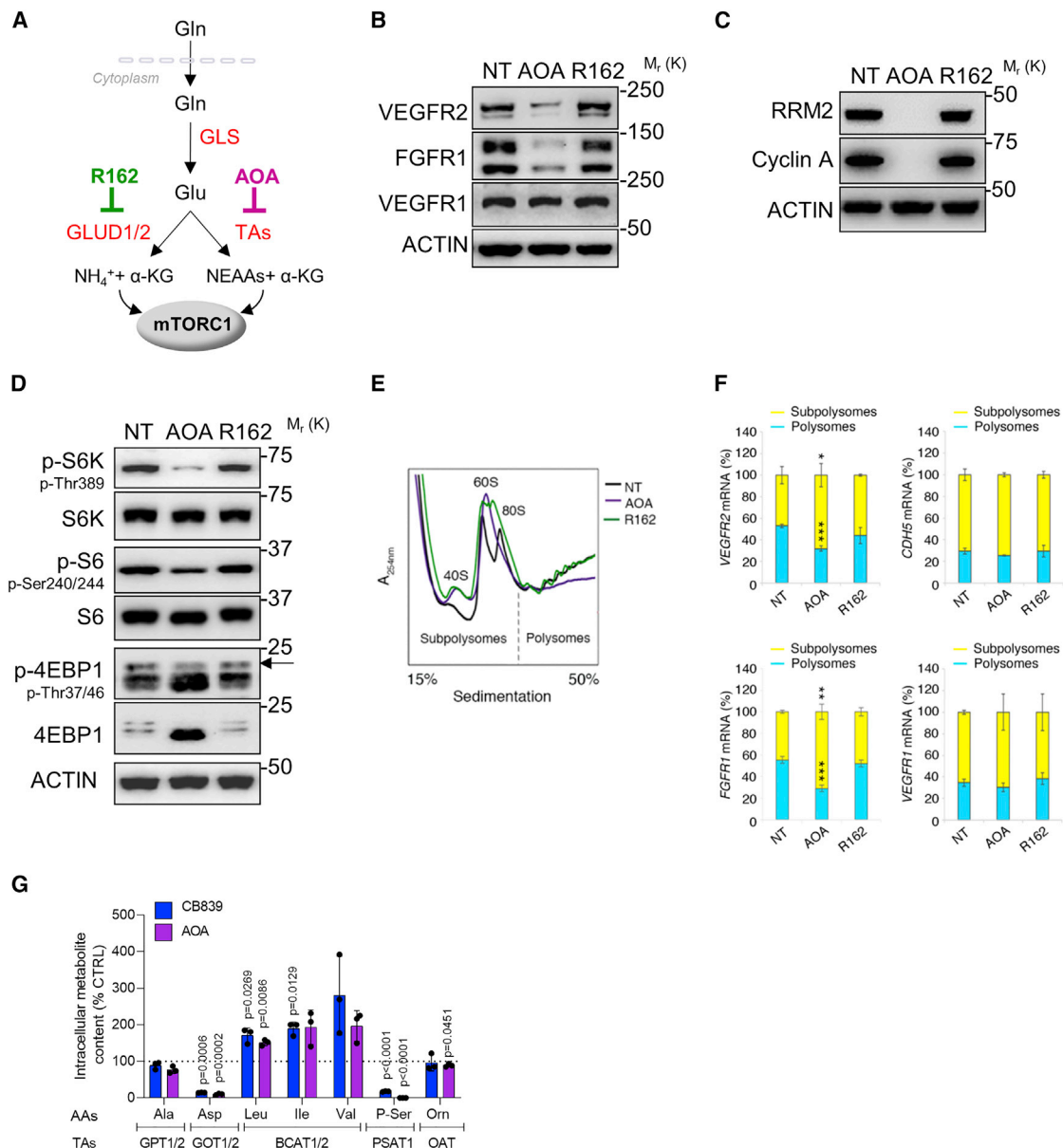
Figure 4. Transaminases-derived Asp is crucial for endothelial growth factor receptors translation and pyrimidine synthesis in ECs

(A) Schematic representation of Glu catabolism. Glu is metabolized by Glu dehydrogenases 1 and 2 (GLUD1/2) to α-ketoglutarate and ammonium, enzymatic reaction inhibited by R162. Moreover, Glu can be converted into NEAAs and α-ketoglutarate by transaminases (TAs) which are inhibited with aminooxyacetate acid (AOA).

(B) Immunoblot analysis of VEGFR2, FGFR1, and VEGFR1 in ECs treated with 2 mM AOA or 20 μM R162 during 24 h.

(C) Representative immunoblots of RRM2 and cyclin A levels in ECs treated with 2 mM AOA or 20 μM R162 during 24 h.

(D) Analysis of mTORC1 signaling: S6K (p-Thr389 and total), S6 (p-Ser240/244 and total), and 4EBP1 (p-Thr37/46 and total); in ECs treated with 2 mM AOA or 20 μM R162 during 24 h.

(E) Polysome profiles of ECs untreated (NT) or treated with 2 mM AOA or 20 μM R162 for 24 h.

(F) Quantification of mRNA levels in subpolysome and polysome fractions of VEGFR2, FGFR1, CDH5, and VEGFR1 in ECs untreated or treated with 2 mM AOA or 20 μM R162 for 24 h. p values are determined by two-tailed Student's t test.

(G) Intracellular content of alanine (Ala), aspartate (Asp), leucine (Leu), isoleucine (Ile), valine (Val), phosphoserine (P-Ser), and ornithine (Orn) in ECs treated with 200 nM CB839 or 2 mM AOA for 24 h. Data are expressed as % of control (mean ± SD) of three independent experiments. For each independent experiment three wells/conditions were extracted and analyzed. p values are determined by one sample t test.

See also Figure S7.

AOA-treated cells, showing that Gln, Arg, Met, and Leu as well as α-KG are not limiting substrates in these conditions (Figures S8C and S8D). Furthermore, we also investigated whether P-Ser might rescue mTORC1-dependent protein synthesis (Figure S8E). However, we did not detect a role for P-Ser in AOA-dependent mTORC1 regulation. We also ruled
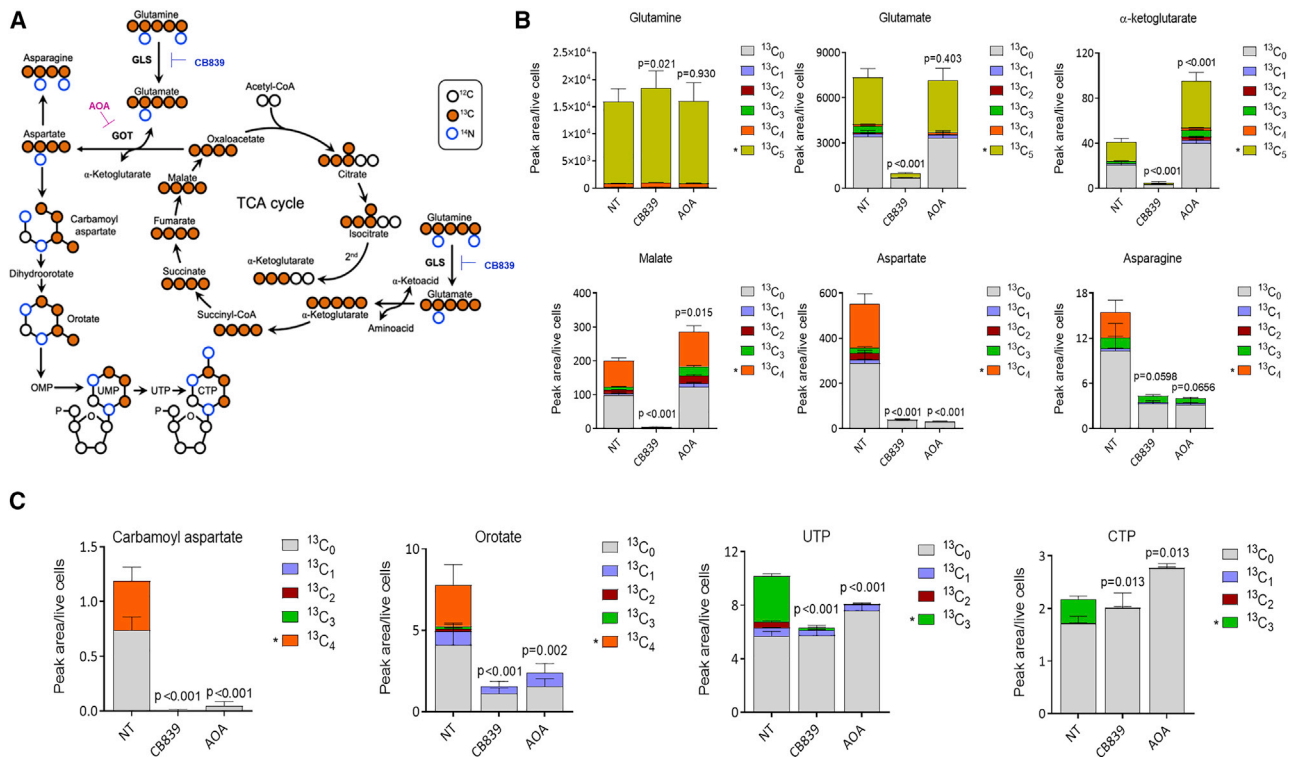
Figure 5. Transaminase-derived Asp is crucial for pyrimidine synthesis in ECs

(A) Schematics of $^{13}C_5$Gln tracing in the tricarboxylic acid (TCA) cycle and *de novo* pyrimidine biosynthesis. The intermediates derived from the first passage in the TCA cycle and the α-ketoglutarate derived from the second passage are shown. For simplicity, only the carbon atoms retained in these pathways are presented, leaving groups and cofactors are omitted.

(B) $^{13}C_5$Gln-derived isotopologs of the TCA cycle and *de novo* pyrimidine biosynthesis intermediates.

(C) Cells were treated with 200 nM CB839 and 2 mM AOA, or untreated for 24 h. p values refer to two-tailed Student's t test that compare the means of the isotopologs indicated by * in treated versus NT. Bars are mean ± SD (n = 3).

out that Glu was involved in the TA-dependent mechanism, since Glu supplementation was not able to rescue VEGFR2/FGFR1 synthesis and mTORC1 activation in AOA-treated cells, while it was able to do so in CB839-treated cells (Figure S8F). We then asked whether α-KG and Asp supplementation could rescue AOA-dependent EC proliferation defects (Figures 6C and 6D). In line with the previous results, Asp, but not α-KG, supplementation was able to restore cell growth and rescue RRM2 and cyclin A levels as well as CAD activation. To validate the relevance of our findings *in vivo*, we tested whether Asp supplementation can restore angiogenesis in the model of mouse retina. We then provide Asp via a single intraocular injection of an aqueous solution of Asp in one eye and vehicle in the other. An intraocular injection of Asp was able to restore the angiogenic defects of $Gls^{i\Delta EC}$ pups, while in $Gls^{fl/fl}$ animals it did not produce any apparent angiogenic phenotype (Figure 6E).

The integrated stress response (ISR) pathway is triggered by specific stresses, and it enhances the translation of specific mRNAs, such as those encoding the transcription factor ATF4 (Holcik and Sonenberg, 2005). It has been shown that amino acid deprivation triggers ISR via the GCN2/eIF2a/ATF4 pathway; on the other hand, it has been demonstrated that ATF4 suppresses mTORC1 activity upon amino acid starvation (Ye et al., 2015). Glutaminolysis (CB839) or TA (AOA) inhibition

activates the ATF4-mediated ISR pathway in ECs (Figure S9A). We next addressed the possibility that Glu, Asp, and Asn can prevent ATF4 induction upon CB839 or AOA treatments. Interestingly, upon glutaminolysis blockade, the supplementation of Glu and Asp, but not Asn alone, was able to rescue ATF4-mediated cell stress. On the contrary, during TA inhibition, only Asp was able to block ATF4 induction (Figure S9A). These results indicate that Asp is required to rescue glutaminolysis (CB839) or TA (AOA) inhibition, suggesting that mTORC1 activation and the related VEGFR2/FGFR1 translation is dependent on Asp levels within the cell. It has been shown that Asn metabolism might play a role in angiogenesis (Huang et al., 2017). We next explored whether Asn supplementation can rescue AOA treatments. Asn alone was able to rescue endothelial growth factor translation and mTORC1 activation and, at least in part, restore cell growth, p-CAD activation, and cyclin A and RRM2 levels in these conditions (Figures S9B–S9E). We also discovered that AOA treatment increased the protein levels of ASNS (Figure S9F), possibly through ATF4 induction, suggesting the possibility that Asn-mediated rescue might occur through its uncanonical conversion to Asp.

Overall, we showed that the Asp-dependent regulation of mTORC1 activity enables VEGFR2/FGFR1 translation and pyrimidine synthesis in ECs. Further experiments will be necessary to clarify how Asn contributes to mTORC1 activation.
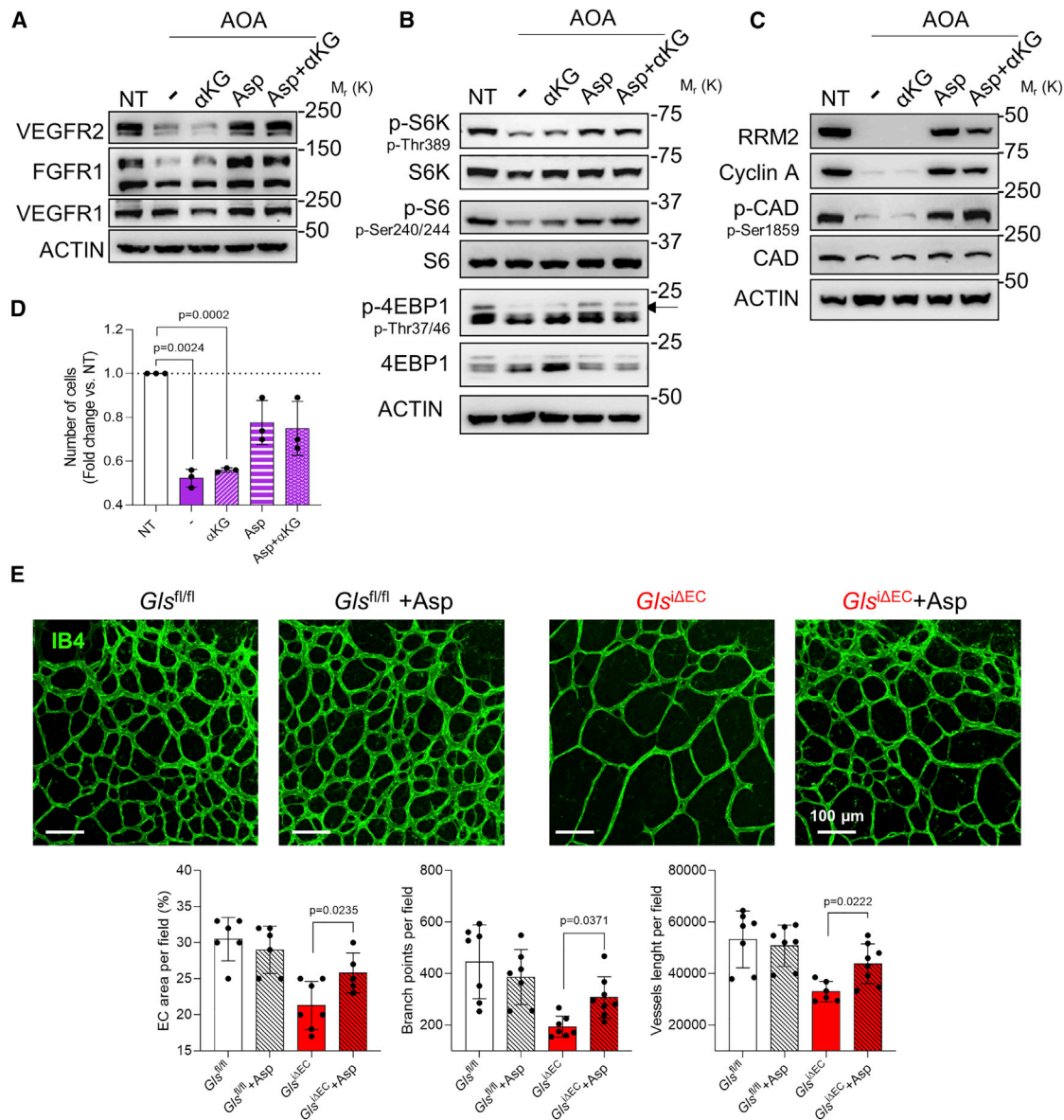
Figure 6. Asp rescue glutaminolysis (CB839) or transaminase (AOA) inhibition

(A) Rescue experiment of VEGFR2, FGFR1, and VEGFR1 using 1 mM dimethyl-2-oxoglutarate (α-KG), 2 mM Asp, or both in ECs treated with 2 mM AOA for 24 h.

(B) Rescue experiment of the mTORC1 pathway using 1 mM dimethyl-2-oxoglutarate (α-KG), 2-mM Asp, or both in ECs treated with 2 mM AOA for 24 h.

(C) Representative immunoblots of RRM2, cyclin A, and p-CAD (p-Ser1859 and total) in ECs treated with 2 mM AOA in the presence of 1 mM dimethyl-2-oxoglutarate (α-KG), 2 mM Asp, or both.

(D) Cell number fold change compare with NT of ECs treated with 2 mM AOA in the presence of 1 mM dimethyl-2-oxoglutarate (α-KG), 2 mM Asp, or both. Data are shown as mean ± SD of n = 3 independent experiments; p values are determined by one-sample t test.

(E) Retinal vasculature analysis of $Gls^{fl/fl}$ and $Gls^{i\Delta EC}$ mice using isolectin B4 staining at postnatal (P) day 7. Asp was injected via intraocular administration at P5 into one eye, and PBS was injected into the contralateral eye as the control. Data are shown as mean ± SEM of n ≥ 6 mice per group. p values are determined by one-way ANOVA test.

See also Figures S8 and S9.

GOT1 controls Asp-dependent mTORC1 activation in ECs

Asp can be synthesized through two different PLP-dependent TAs, AST1/GOT1 and AST2/GOT2. GOTs catalyze the reversible transfer of an α-amino group to or from Asp, and their functions are yet unexplored in ECs. Our findings showed that both GOT1 and GOT2 are expressed by ECs (Figure S10A), and their KD severely affects EC proliferation and markers (Figures 7A and S10B). We then investigated whether these enzymes equally affect Asp-dependent endothelial growth factor receptor synthesis and mTORC1 activation. We found that the GOT1 blockade significantly impaired VEGFR2 and FGFR1 synthesis as well as
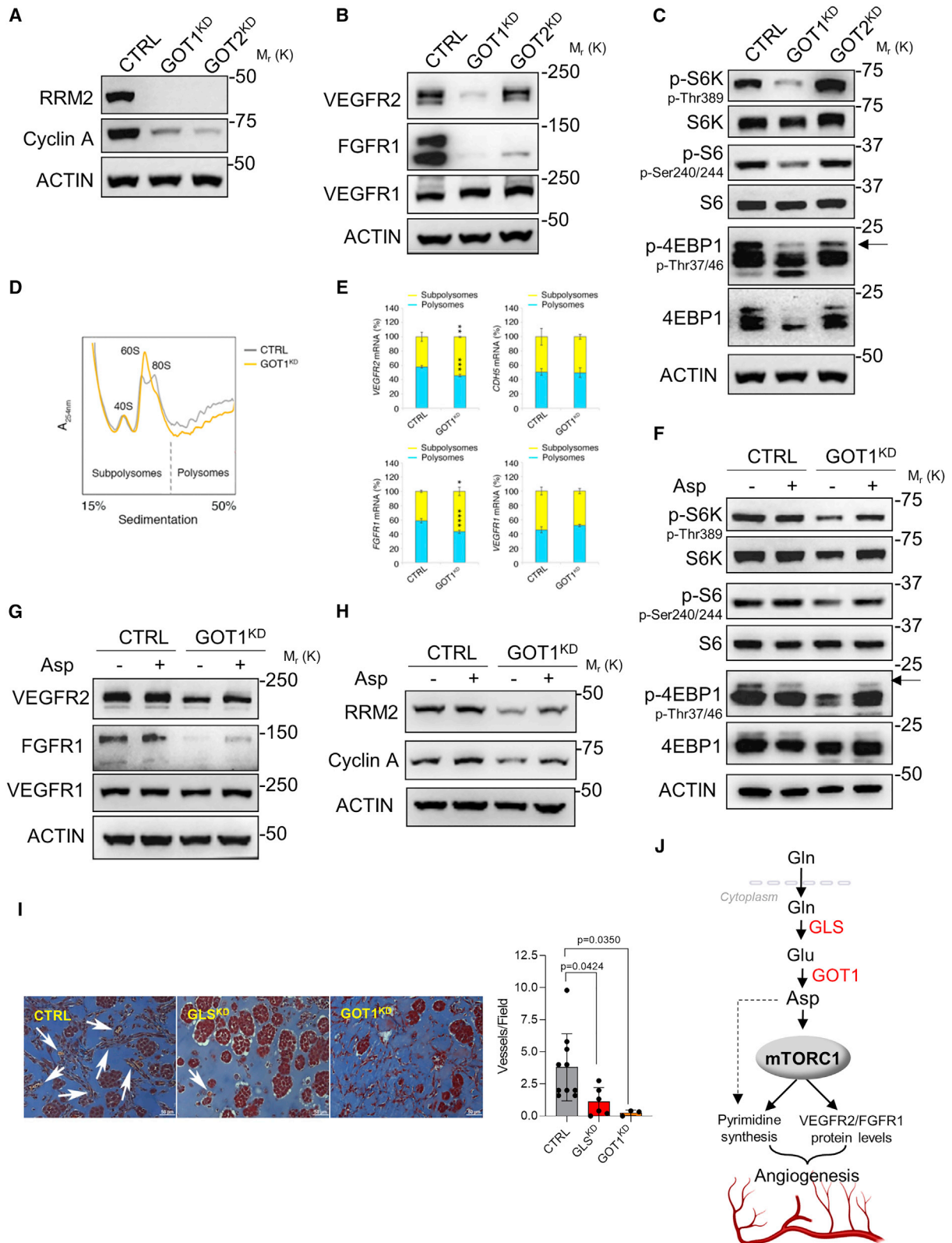
Figure 7. GOT1 controls mTORC1 activation in ECs and is required for *in vivo* angiogenesis

(A) Representative immunoblot of RRM2 and cyclin A in ECs silenced for GOT1 and GOT2.

(B) Immunoblot analysis of VEGFR2, FGFR1, and VEGFR1 in ECs silenced for GOT1 and GOT2.

mTORC1 activation compared with the CTRL (Figures 7B, 7C, S10C, and S10D). Interestingly, GOT2^KD did not show impairment of VEGFR2 synthesis and mTORC1 activation. These data indicated that the cytosolic GOT1 rather than the mitochondrial GOT2 is important in Asp-mediated mTORC1 activation.

Next, we analyzed whether GOT1 blockade might affect EC translation (Figure 7D). Polysomal profiles of GOT1^KD cells showed a reduction of polysome heights with respect to CTRLs. Accordingly, the qRT-PCR analysis of the distribution of VEGFR2 and FGFR1 mRNAs on polysomal fractions of GOT1^KD cells clearly showed a shift of VEGFR2 and FGFR1 mRNAs to non-translating subpolysomal fractions, compared with CTRL cells (Figure 7E).

To confirm the role of Asp in mTORC1 activation, we assessed whether Asp supplementation could rescue mTORC1-driven endothelial growth factor receptor and RRM2 and cyclin A level defects in GOT1^KD cells (Figures 7F–7H, S10E, and S10F); nevertheless, to different extents, Asp supplementation alone was sufficient to restore mTORC1 signaling activation, VEGFR2 and FGFR1 synthesis, and cell proliferation markers.

Lastly, to assess the effect of GOT1 *in vivo*, we used a matrigel plug angiogenesis assay induced by human TECs implanted subcutaneously in mice with severe combined immunodeficiency (SCID mice) within the matrigel (Bussolati et al., 2003). In this model, human TECs organize in structures connected with the mouse circulation (Lopatina et al., 2019). TECs were silenced by lentiviral infection for GLS and GOT1 (Figure S10G) and injected subcutaneously within the diluted matrigel in SCID mice. Seven days after implantation, matrigel plugs were excised and vessel density analyzed by trichrome staining. The analysis of CTRL plugs showed the presence of erythrocyte-containing vessels, while plugs of GLS^KD and GOT1^KD TECs did not present vessels (Figure 7I). Overall, we can conclude that GLS, as well as GOT1, is required to drive angiogenesis *in vivo*.

Our data demonstrate that angiogenic ECs engage carbon and nitrogen metabolism by simultaneously promoting the GLS-dependent Gln anaplerosis and GOT-dependent Asp synthesis that is required to activate the mTORC1 pathway which, in turn, promotes the endothelial growth factor receptor translation and pyrimidine synthesis required to support developmental and pathological angiogenesis (Figure 7J).

DISCUSSION

Here, we show a mechanism through which glutaminolysis-derived Asp coordinates endothelial growth factor receptor translation and protein levels via mTORC1 signaling in ECs. These findings demonstrate how nutrients, such as amino acids, regulate growth factor signaling during angiogenesis. Such metabolic control of growth factor receptors becomes mandatory to orchestrate key steps in the angiogenesis process such as EC proliferation in pathological settings.

The role of mTORC1 signaling during angiogenesis has been poorly investigated in ECs (Karali et al., 2014). Here, we found that Asp metabolism regulates mTORC1 signaling in ECs and, in turn, controls the angiogenic response. How Asp might signal to mTORC1 in ECs is not known and needs further investigation, including its conversion to Asn through ASNS. It has been shown that Asp synthesis is critical in cancer cell autonomous proliferation because Asp is essential not only for protein synthesis but also for nucleotide biosynthesis in proliferating cells (Birsoy et al., 2015; Sullivan et al., 2015). Circulating levels of Asp are low compared with other amino acids, and it is assumed that cells largely rely on intracellular Asp biosynthesis to sustain cellular growth. Asp biosynthesis is largely driven by the Asp TAs GOT1 and GOT2. Studies on the function of Asp TAs in ECs are still missing. Interestingly, previous work focusing on the role of vascular stiffness and cellular metabolism in pulmonary hypertension (PH) identified YAP/TAZ activation as a direct way to modulate glutaminolysis and GLS in ECs (Bertero et al., 2016). Here, it has been shown that glutaminolysis is required to replenish Asp for sustaining endothelial proliferation and migration, and in agreement with our data, the authors also showed that Asp addition to GLS-inhibited cells restored EC proliferation (Bertero et al., 2016). Another recent study supports a role for the cytosolic form of AST/GOT in mTORC activation in fission yeast (Reidman et al., 2019). We highlight here that TAs such as GOT1 might play a functional role in angiogenesis by activating mTORC1 signaling. Further investigation is needed to understand the different function of cytosolic versus mitochondrial Asp and malate-Asp shuttle during angiogenesis and mTORC1 signaling.

In terms of potential therapeutical strategies, both Glu production (via glutaminolysis) and Glu catabolism (via Asp synthesis) can be targeted. Inhibition of glutaminolysis for the treatment of numerous types of cancer has been widely investigated in the recent years. As of today, different glutaminolysis inhibitors, such as CB839, are used in combination with anti-growth factor receptor inhibitors (including bevacizumab and VEGFR2 inhibitor) in clinical trials (Huang et al., 2018; Meric-Bernstam et al., 2019; Raczka and Reynolds, 2019; Tannir et al., 2019; Yang et al., 2017). Recently, few compounds showing inhibitory activity toward

---

(C) Immunoblot analysis of mTORC1 signaling: S6K (p-Thr389 and total), S6 (p-Ser240/244 and total), and 4EBP1 (p-Thr37/46 and total); in ECs silenced for GOT1 and GOT2.

(D) Polysome profiles of EC control (CTRL) and KD for GOT1.

(E) Quantification of mRNA levels in subpolysome and polysome fractions of: VEGFR2, FGFR1, CDH5, and VEGFR1, in ECs silenced for GOT1. Data are presented as mean ± SD of technical triplicates; p values are determined by two-tailed Student's t test.

(F) Rescue experiment of the mTORC1 pathway using 2 mM Asp in CTRL and GOT1^KD EC.

(G) Rescue experiment of VEGFR2, FGFR1, and VEGFR1 using 2 mM Asp in GOT1^KD EC.

(H) Representative immunoblots of RRM2 and cyclin A of CTRL and GOT1^KD in presence or absence of 2 mM Asp.

(I) Matrigel plug angiogenesis assay. Representative images of plug sections, stained with Masson's trichomic reaction (extracellular matrix is stained in blue, cells in red, and erythrocytes in orange). Vessels are indicated by arrows. Quantification of vessels /field of plugs containing CTRL, GLS^KD, and GOT1^KD TEC. Data are shown as mean ± SD of n ≥ 3 mice per group. Statistics were assessed using one-way ANOVA test. Scale bars, 50 μm.

(J) A schematic representation showing endothelial GLS-derived Glu activates mTORC1 signaling to support endothelial growth factor receptors (VEGFR2 and FGFR1) translation and pyrimidine synthesis through Asp synthesis by GOT1 during angiogenesis.

See also Figure S10.

GOT1 activity and causing GOT1-dependent impairment of pancreatic cancer growth have been identified (Sun et al., 2019; Yoshida et al., 2020). Altogether, these findings might be attractive for developing strategies to inhibit pathological angiogenesis and provide an important avenue for improving the efficacy of anti-angiogenic therapy and blocking adaptive resistance.

Limitations of the study

A limitation of this study is that we do not comprehend why Asp-dependent mTOR activation affects endothelial growth factor receptor translation differently such as VEGFR1 versus VEGFR2. To investigate how different nutrients regulate the mTORC pathway and translation in ECs, functional translatome proteomics and ribosome- versus polysome-profiling followed by RNA sequencing studies might help (Gandin et al., 2016; Klann et al., 2020). Another limitation is the difficulty in evaluating the role of cytosolic versus mitochondrial Asp pools produced by GOT1 versus GOT2, respectively. Mass spectrometry imaging technology will help in resolving this issue during angiogenesis.

STAR★METHODS

Detailed methods are provided in the online version of this paper and include the following:

- KEY RESOURCES TABLE
- RESOURCE AVAILABILITY
  - Lead contact
  - Materials availability
  - Data and code availability
- EXPERIMENTAL MODEL AND SUBJECT DETAILS
  - Cell culture
  - Mouse model
- METHOD DETAILS
  - Virus transduction
  - Cell viability assay
  - Cytometric analysis of cell cycle
  - Real time q-PCR
  - Western blotting
  - Glutamine deprivation and rescue experiments
  - Metabolite's extraction and quantification
  - Immunofluorescence analyses
  - Subcellular fractionation experiments
  - Biotinylation experiments
  - Allograft experiments
  - Isolation of mouse tumor EC
  - Cytometric quantification of TEC
  - Isolation of micropulmonary of EC
  - Hindlimb ischemia model
  - Retinal angiogenesis and quantification
  - Polysomal profile analysis
  - Proteomic analysis
  - Matrigel plug angiogenesis assay
- QUANTIFICATION AND STATISTICAL ANALYSIS

SUPPLEMENTAL INFORMATION

Supplemental information can be found online at https://doi.org/10.1016/j.devcel.2022.04.018.

AUTHOR CONTRIBUTIONS

R.E.O. and M.M.S. conceived the concept of the study. M.M.S. provided supervision and wrote the manuscript. M.M.S., R.E.O., G.P., E.P., and S.T. were involved in the experimental design. M.F.A. and S.T. performed the metabolomics analyses. R.E.O., G.P., and G.T. carried out biological activity assays. R.E.O., L.A., and M.S. undertook tumor xenograft experiments. M.A. and R.E.O. performed retina angiogenesis experiments. R.E.O., G.P., and E.P. performed cell culture experiments. P.G. performed and analyzed proteomic data. S.R. and S.B. performed and analyzed polysomal profile assays. A.B. and B.B. performed plug angiogenesis assays. R.E.O., S.T., S.B., P.G., B.B., and M.M.S. interpreted the data. All authors agreed on the final version of the manuscript. All authors commented on the manuscript.

DECLARATION OF INTERESTS

The authors declare no competing interests.

REFERENCES

Altman, B.J., Stine, Z.E., and Dang, C.V. (2016). From Krebs to clinic: glutamine metabolism to cancer therapy. Nat. Rev. Cancer *16*, 619–634.

Apte, R.S., Chen, D.S., and Ferrara, N. (2019). VEGF in signaling and disease: Beyond discovery and development. Cell *176*, 1248–1264.

Arsic, N., Zacchigna, S., Zentilin, L., Ramirez-Correa, G., Pattarini, L., Salvi, A., Sinagra, G., and Giacca, M. (2004). Vascular endothelial growth factor stimulates skeletal muscle regeneration *in vivo*. Mol. Ther. *10*, 844–854.

Ben-Sahra, I., Howell, J.J., Asara, J.M., and Manning, B.D. (2013). Stimulation of *de novo* pyrimidine synthesis by growth signaling through mTOR and S6K1. Science *339*, 1323–1328.

Ben-Sahra, I., and Manning, B.D. (2017). mTORC1 signaling and the metabolic control of cell growth. Curr. Opin. Cell Biol. *45*, 72–82.

Bertero, T., Oldham, W.M., Cottrill, K.A., Pisano, S., Vanderpool, R.R., Yu, Q., Zhao, J., Tai, Y., Tang, Y., Zhang, Y.Y., et al. (2016). Vascular stiffness mechanoactivates YAP/TAZ-dependent glutaminolysis to drive pulmonary hypertension. J. Clin. Invest. *126*, 3313–3335.

Birsoy, K., Wang, T., Chen, W.W., Freinkman, E., Abu-Remaileh, M., and Sabatini, D.M. (2015). An essential role of the mitochondrial electron transport chain in cell proliferation is to enable aspartate synthesis. Cell *162*, 540–551.

Bussolati, B., Deambrosis, I., Russo, S., Deregibus, M.C., and Camussi, G. (2003). Altered angiogenesis and survival in human tumor-derived endothelial cells. FASEB J. *17*, 1159–1161.

Chandel, N.S. (2021). Nucleotide metabolism. Cold Spring Harb. Perspect. Biol. *13*, a040592.

Choo, A.Y., Yoon, S.O., Kim, S.G., Roux, P.P., and Blenis, J. (2008). Rapamycin differentially inhibits S6Ks and 4E-BP1 to mediate cell-type-specific repression of mRNA translation. Proc. Natl. Acad. Sci. USA *105*, 17414–17419.

Claxton, S., Kostourou, V., Jadeja, S., Chambon, P., Hodivala-Dilke, K., and Fruttiger, M. (2008). Efficient, inducible Cre-recombinase activation in vascular endothelium. Genesis *46*, 74–80.

Diebold, L.P., Gil, H.J., Gao, P., Martinez, C.A., Weinberg, S.E., and Chandel, N.S. (2019). Mitochondrial complex III is necessary for endothelial cell proliferation during angiogenesis. Nat. Metab. *1*, 158–171.

Durán, R.V., Oppliger, W., Robitaille, A.M., Heiserich, L., Skendaj, R., Gottlieb, E., and Hall, M.N. (2012). Glutaminolysis activates Rag-mTORC1 signaling. Mol. Cell *47*, 349–358.

Gallo-Oller, G., Ordoñez, R., and Dotor, J. (2018). A new background subtraction method for Western blot densitometry band quantification through image analysis software. J. Immunol. Methods *457*, 1–5.

Gandin, V., Masvidal, L., Hulea, L., Gravel, S.P., Cargnello, M., McLaughlan, S., Cai, Y., Balanathan, P., Morita, M., Rajakumar, A., et al. (2016). nanoCAGE reveals 5′ UTR features that define specific modes of translation of functionally related MTOR-sensitive mRNAs. Genome Res. *26*, 636–648.

Grange, C., Bussolati, B., Bruno, S., Fonsato, V., Sapino, A., and Camussi, G. (2006). Isolation and characterization of human breast tumor-derived endothelial cells. Oncol. Rep. *15*, 381–386.

Hagberg, C.E., Falkevall, A., Wang, X., Larsson, E., Huusko, J., Nilsson, I., van Meeteren, L.A., Samen, E., Lu, L., Vanwildemeersch, M., et al. (2010). Vascular endothelial growth factor B controls endothelial fatty acid uptake. Nature *464*, 917–921.

Holcik, M., and Sonenberg, N. (2005). Translational control in stress and apoptosis. Nat. Rev. Mol. Cell Biol. *6*, 318–327.

Huang, H., Vandekeere, S., Kalucka, J., Bierhansl, L., Zecchin, A., Brüning, U., Visnagri, A., Yuldasheva, N., Goveia, J., Cruys, B., et al. (2017). Role of glutamine and interlinked asparagine metabolism in vessel formation. EMBO J. *36*, 2334–2352.

Huang, Q., Stalnecker, C., Zhang, C., McDermott, L.A., Iyer, P., O'Neill, J., Reimer, S., Cerione, R.A., and Katt, W.P. (2018). Characterization of the interactions of potent allosteric inhibitors with glutaminase C, a key enzyme in cancer cell glutamine metabolism. J. Biol. Chem. *293*, 3535–3545.

Jin, L., Li, D., Alesi, G.N., Fan, J., Kang, H.B., Lu, Z., Boggon, T.J., Jin, P., Yi, H., Wright, E.R., et al. (2015). Glutamate dehydrogenase 1 signals through antioxidant glutathione peroxidase 1 to regulate redox homeostasis and tumor growth. Cancer Cell *27*, 257–270.

Karali, E., Bellou, S., Stellas, D., Klinakis, A., Murphy, C., and Fotsis, T. (2014). VEGF signaling, mTOR complexes, and the endoplasmic reticulum: Towards a role of metabolic sensing in the regulation of angiogenesis. Mol. Cell. Oncol. *1*, e964024.

Kim, B., Li, J., Jang, C., and Arany, Z. (2017). Glutamine fuels proliferation but not migration of endothelial cells. EMBO J. *36*, 2321–2333.

Kim, E., Goraksha-Hicks, P., Li, L., Neufeld, T.P., and Guan, K.-L. (2008). Regulation of TORC1 by Rag GTPases in nutrient response. Nat. Cell Biol. *10*, 935–945.

Klann, K., Tascher, G., and Münch, C. (2020). Functional Translatome proteomics reveal converging and dose-dependent regulation by mTORC1 and eIF2alpha. Mol. Cell *77*, 913–925.e4.

Li, X., Sun, X., and Carmeliet, P. (2019). Hallmarks of endothelial cell metabolism in health and disease. Cell Metab. *30*, 414–433.

Limbourg, A., Korff, T., Napp, L.C., Schaper, W., Drexler, H., and Limbourg, F.P. (2009). Evaluation of postnatal arteriogenesis and angiogenesis in a mouse model of hind-limb ischemia. Nat. Protoc. *4*, 1737–1746.

Longchamp, A., Mirabella, T., Arduini, A., MacArthur, M.R., Das, A., Treviño-Villarreal, J.H., Hine, C., Ben-Sahra, I., Knudsen, N.H., Brace, L.E., et al. (2018). Amino acid restriction triggers angiogenesis via GCN2/ATF4 regulation of VEGF and H2S production. Cell *173*, 117–129.e14.

Lopatina, T., Grange, C., Fonsato, V., Tapparo, M., Brossa, A., Fallo, S., Pitino, A., Herrera-Sanchez, M.B., Kholia, S., Camussi, G., et al. (2019). Extracellular vesicles from human liver stem cells inhibit tumor angiogenesis. Int. J. Cancer *144*, 322–333.

Ma, X.M., and Blenis, J. (2009). Molecular mechanisms of mTOR-mediated translational control. Nat. Rev. Mol. Cell Biol. *10*, 307–318.

Meric-Bernstam, F., Lee, R.J., Carthon, B.C., Iliopoulos, O., Mier, J.W., Patel, M.R., Tannir, N.M., Owonikoko, T.K., Haas, N.B., Voss, M.H., et al. (2019). CB-839, a glutaminase inhibitor, in combination with cabozantinib in patients with clear cell and papillary metastatic renal cell cancer (mRCC): results of a phase I study. J. Clin. Oncol. *37*, 549.

Michalski, A., Damoc, E., Hauschild, J.P., Lange, O., Wieghaus, A., Makarov, A., Nagaraj, N., Cox, J., Mann, M., and Horning, S. (2011). Mass spectrometry-based proteomics using Q Exactive, a high-performance benchtop quadrupole Orbitrap mass spectrometer. Mol. Cell. Proteomics *10*. M111.011015.

Mingote, S., Masson, J., Gellman, C., Thomsen, G.M., Lin, C.S., Merker, R.J., Gaisler-Salomon, I., Wang, Y., Ernst, R., Hen, R., et al. (2015). Genetic pharmacotherapy as an early CNS drug development strategy: testing glutaminase inhibition for schizophrenia treatment in adult mice. Front. Syst. Neurosci. *9*, 165.

Monvoisin, A., Alva, J.A., Hofmann, J.J., Zovein, A.C., Lane, T.F., and Iruela-Arispe, M.L. (2006). VE-cadherin-CreERT2 transgenic mouse: a model for inducible recombination in the endothelium. Dev. Dyn. *235*, 3413–3422.

Mossmann, D., Park, S., and Hall, M.N. (2018). mTOR signalling and cellular metabolism are mutual determinants in cancer. Nat. Rev. Cancer *18*, 744–757.

Napolitano, G., Di Malta, C., Esposito, A., de Araujo, M.E.G., Pece, S., Bertalot, G., Matarese, M., Benedetti, V., Zampelli, A., Stasyk, T., et al. (2020). A substrate-specific mTORC1 pathway underlies Birt–Hogg–Dubé syndrome. Nature *585*, 597–602.

Nordlund, P., and Reichard, P. (2006). Ribonucleotide reductases. Annu. Rev. Biochem. *75*, 681–706.

Palm, W., and Thompson, C.B. (2017). Nutrient acquisition strategies of mammalian cells. Nature *546*, 234–242.

Panda, A.C., Martindale, J.L., and Gorospe, M. (2017). Polysome fractionation to analyze mRNA distribution profiles. Bio Protoc. *7*, e2126.

Potente, M., and Mäkinen, T. (2017). Vascular heterogeneity and specialization in development and disease. Nat. Rev. Mol. Cell Biol. *18*, 477–494.

Rappsilber, J., Ishihama, Y., and Mann, M. (2003). Stop and go extraction tips for matrix-assisted laser desorption/ionization, nanoelectrospray, and LC/MS sample pretreatment in proteomics. Anal. Chem. *75*, 663–670.

Reidman, S., Cohen, A., Kupiec, M., and Weisman, R. (2019). The cytosolic form of aspartate aminotransferase is required for full activation of TOR complex 1 in fission yeast. J. Biol. Chem. *294*, 18244–18255.

Raczka, A.M., and Reynolds, P.A. (2019). Glutaminase inhibition in renal cell carcinoma therapy. Cancer Drug Resist. *2*, 356–364.

Ricciardi, S., Manfrini, N., Alfieri, R., Calamita, P., Crosti, M.C., Gallo, S., Müller, R., Pagani, M., Abrignani, S., and Biffo, S. (2018). The translational machinery of human CD4(+) T cells is poised for activation and controls the switch from quiescence to metabolic remodeling. Cell Metab. *28*, 961.

Robitaille, A.M., Christen, S., Shimobayashi, M., Cornu, M., Fava, L.L., Moes, S., Prescianotto-Baschong, C., Sauer, U., Jenoe, P., and Hall, M.N. (2013). Quantitative phosphoproteomics reveal mTORC1 activates *de novo* pyrimidine synthesis. Science *339*, 1320–1323.

Saxton, R.A., and Sabatini, D.M. (2017). MTOR signaling in growth, metabolism, and disease. Cell *168*, 960–976.

Sullivan, L.B., Gui, D.Y., Hosios, A.M., Bush, L.N., Freinkman, E., and Vander Heiden, M.G. (2015). Supporting aspartate biosynthesis is an essential function of respiration in proliferating cells. Cell *162*, 552–563.

Sun, W., Luan, S., Qi, C., Tong, Q., Yan, S., Li, H., and Zhang, Y. (2019). Aspulvinone O, a natural inhibitor of GOT1 suppresses pancreatic ductal adenocarcinoma cells growth by interfering glutamine metabolism. Cell Commun. Signal. *17*, 111.

Tannir, N.M., Agarwal, N., Dawson, N.A., Motzer, R.J., Jacobs, C.M., Choueiri, T.K., Hrom, J.S., Geynisman, D.M., Davis, N.B., Figlin, R.A., et al. (2019). CANTATA: randomized, international, double-blind study of CB-839 plus cabozantinib versus cabozantinib plus placebo in patients with metastatic renal cell carcinoma. J. Clin. Oncol. *37*, TPS682.

Thornburg, J.M., Nelson, K.K., Clem, B.F., Lane, A.N., Arumugam, S., Simmons, A., Eaton, J.W., Telang, S., and Chesney, J. (2008). Targeting aspartate aminotransferase in breast cancer. Breast Cancer Res. *10*, R84.

Tong, X., Zhao, F., and Thompson, C.B. (2009). The molecular determinants of *de novo* nucleotide biosynthesis in cancer cells. Curr. Opin. Genet. Dev. *19*, 32–37.

Vande Voorde, J., Ackermann, T., Pfetzer, N., Sumpton, D., Mackay, G., Kalna, G., Nixon, C., Blyth, K., Gottlieb, E., and Tardito, S. (2019). Improving the metabolic fidelity of cancer models with a physiological cell culture medium. Sci. Adv. *5*, eaau7314.

Yang, L., Venneti, S., and Nagrath, D. (2017). Glutaminolysis: a hallmark of cancer metabolism. Annu. Rev. Biomed. Eng. *19*, 163–194.

Ye, J., Palm, W., Peng, M., King, B., Lindsten, T., Li, M.O., Koumenis, C., and Thompson, C.B. (2015). GCN2 sustains mTORC1 suppression upon amino acid deprivation by inducing Sestrin2. Genes Dev. *29*, 2331–2336.

Yoshida, T., Yamasaki, S., Kaneko, O., Taoka, N., Tomimoto, Y., Namatame, I., Yahata, T., Kuromitsu, S., Cantley, L.C., and Lyssiotis, C.A. (2020). A covalent small molecule inhibitor of glutamate-oxaloacetate transaminase 1 impairs pancreatic cancer growth. Biochem. Biophys. Res. Commun. *522*, 633–638.

Yu, P., Wilhelm, K., Dubrac, A., Tung, J.K., Alves, T.C., Fang, J.S., Xie, Y., Zhu, J., Chen, Z., De Smet, F., et al. (2017). FGF-dependent metabolic control of vascular development. Nature *545*, 224–228.

Zudaire, E., Gambardella, L., Kurcz, C., and Vermeren, S. (2011). A computational tool for quantitative analysis of vascular networks. PLoS One *6*, e27385.

STAR★METHODS

KEY RESOURCES TABLE

Reagent or resource	Source	Identifier
Antibodies		
Rabbit polyclonal anti-ASNS	Cell SignalingTechnology	Cat. #20843
Rabbit polyclonal anti-COXIV	Abcam	Cat.#ab16056; RRID: AB_443304
Rabbit polyclonal anti-Glutaminase	Abcam	Cat.#ab93434; RRID: AB_10561964
Rabbit monoclonal anti-GLUD1 (clone EPR11369(B))	Abcam	Cat.#ab166618; RRID: AB_2815030
Mouse polyclonal anti-GLUD2	Abcam	Cat. #ab88519; RRID: AB_2041423
Rabbit monoclonal anti-GOT1 (clone E4A40)	Cell SignalingTechnology	Cat. #34423
Rabbit polyclonal anti-GOT2	Thermo Fisher Scientific	Cat. #77990; RRID: AB_2735868
Rabbit polyclonal anti-KLF2	Millipore	Cat. # 09-820; RRID: AB_10807287
Rabbit polyclonal anti-PSAT1	Abcam	Cat. #ab96136; RRID: AB_10697763
Mouse monoclonal anti-Vinculin (clone HVIN-1)	Sigma-Aldrich	Cat.#V9131; RRID: AB_477629
Rat monoclonal anti-CD31 (clone SZ31)	Dianova	Cat.#DIA-310; RRID: AB_2631039
Rat monoclonal anti-Mouse CD31 (clone MEC 13.3)	BD Pharmingen™	Cat.#550274 RRID: AB_393571
Mouse monoclonal anti-Alpha-Smooth Muscle Actin	Dako	Cat.#M0851; RRID: AB_2223500
Rabbit monoclonal anti-VEGF Receptor 2 (clone D5B1)	Cell Signaling Technology	Cat.#9698; RRID: AB_11178792
Rabbit monoclonal anti Phospho-VEGF Receptor 2 (Tyr1175) (clone 19A10)	Cell Signaling Technology	Cat.#2478; RRID: AB_331377
Goat polyclonal anti-VE-Cadherin	R and D Systems	Cat.#AF938; RRID: AB_355726
Rabbit polyclonal anti-VE-Cadherin	Cayman Chemical	Cat.#160840; RRID: AB_10077705
Rabbit monoclonal anti-FGFR1 (clone D8E4)	Cell Signaling Technology	Cat.#9740; RRID: AB_11178519
Rabbit Monoclonal VEGFR1 (Cone Y103)	Abcam	Cat. #32152; RRID: AB_778798
Mouse monoclonal anti-Beta-Actin (clone AC74)	Sigma-Aldrich	Cat.#A5316; RRID: AB_476743
Rabbit monoclonal anti-ATF4 (clone D4B8)	Cell Signaling Technology	Cat.#11815; RRID: AB_2616025
Rabbit polyclonal anti-p44/42 MAP kinase (phosphorylated Erk1/2)	Cell Signaling Technology	Cat.#9101; RRID: AB_331646
Mouse monoclonal anti-Erk1/2 (clone C-9)	Santa Cruz Biotechnology	Cat.#sc514302; RRID: AB_2571739
Rabbit polyclonal anti-p-p38(Thr180/Tyr182)-R	Santa Cruz Biotechnology	Cat.#sc17852-R; RRID: AB_2139810
Rabbit polyclonal anti-p38 MAPK	Cell Signaling Technology	Cat.#9212; RRID:AB_330713
Mouse monoclonal anti-Phospho-Akt (Ser473) (clone 587F11)	Cell Signaling Technology	Cat.#4051; RRID:AB_331158
Rabbit polyclonal anti-Akt	Cell Signaling Technology	Cat.#9272; RRID: AB_329827
Rabbit monoclonal anti-p70 S6 Kinase (clone 49D7)	Cell Signaling Technology	Cat.#2708; RRID: AB_390722
Rabbit monoclonal anti-Phospho-p70 S6 Kinase (Thr389) (clone 108D2)	Cell Signaling Technology	Cat.#9234; RRID: AB_2269803
Rabbit polyclonal anti-p70 S6 Kinase	Cell Signaling Technology	Cat.#2708; RRID: AB_390722
Rabbit monoclonal anti-Phospho-S6 Ribosomal Protein (Ser235/236) (D57.2.2E) XP	Cell Signaling Technology	Cat.#4858; RRID: AB_916156

(Continued on next page)

Continued

Reagent or resource	Source	Identifier
Rabbit monoclonal anti-S6 Ribosomal Protein (clone 5610)	Cell Signaling Technology	Cat.#2217; RRID: AB_331355
Rabbit polyclonal anti-Phospho-4E-BP1 (Thr37/46)	Cell Signaling Technology	Cat.#9459; RRID: AB_330985
Rabbit polyclonal anti-Phospho-4E-BP1 (Ser65)	Cell Signaling Technology	Cat.#9451; RRID: AB_330947
Rabbit polyclonal anti-4E-BP1	Cell Signaling Technology	Cat.#9452; RRID: AB_331692
Rabbit monoclonal anti-Phospho-CAD (Ser1859) (D5K5W)	Cell Signaling Technology	Cat.#67235; RRID: AB_2799722
Rabbit monoclonal anti-CAD (clone D2T8H)	Cell Signaling Technology	Cat. #93925; RRID: AB_2750933
Rabbit polyclonal anti-LC3B	Cell Signaling Technology	Cat.#2775; RRID: AB_915950
Mouse monoclonal anti-cyclin A (clone CY-A1)	Sigma-Aldrich	Cat.#C4710; RRID: AB_1078603
Rabbit monoclonal anti-RRM2 (E7Y9J) XP	Cell Signaling Technology	Cat.#65939
Rabbit polyclonal anti-p27Kip1	Cell Signaling Technology	Cat.#2552; RRID: AB_10693314
Mouse anti-PhosphoHistone 3 (Ser10)	Millipore	Cat. #06-570; RRID: AB_310177
Rabbit monoclonal anti-cleaved caspase-3	Cell SignalingTechnology	Cat. #9664
Donkey anti-Rat IgG (H+L)Alexa Fluor 488	Thermo Fisher Scientific	Cat. #A-21208; RRID: AB_141709
Goat anti-Mouse igG(H+L) Alexa Fluor 568	Thermo Fisher Scientific	Cat. #A11004; RRID: AB_2534072
Goat anti-Rabbit IgG (H+L) Alexa Fluor 488, cross-adsorbed polyclonal	Thermo Fisher Scientific	Cat.#A-11008; RRID: AB_143165
Goat anti-Rabbit IgG (H+L) Alexa Fluor 568, polyclonal	Thermo Fisher Scientific	Cat. #A-11036; RRID: AB_10563566
Goat anti-Rat IgG (H+L) Alexa Fluor 568, cross-adsorbed polyclonal	Thermo Fisher Scientific	Cat.#A-11077; RRID: AB_2534121
Goat anti-Rabbit IgG-HRP, polyclonal	Sigma-Aldrich	Cat.#A6154; RRID: AB_258284
Goat anti-Mouse IgG-HRP, polyclonal	Sigma-Aldrich	Cat.#A4416; RRID: AB_258167
Rabbit anti-Goat IgG-HRP, polyclonal	Sigma-Aldrich	Cat.#A8919; RRID: AB_258425
APC Rat anti-Mouse CD31 (clone MEC 13.3)	BD Pharmingen™	Cat. #551262; RRID: AB_398497
PE-Cyanine 7 anti-Mouse CD45.2 (clone 104)	Thermo Fisher Scientific	Cat. #25-0454-82;RRID: AB_2573350
Chemicals, peptides, and recombinant proteins		
CB-839	Aurogene	Cat. #S-7655
Crystal Violet	Sigma-Aldrich	Cat. #C6158
Propidium iodide	Sigma-Aldrich	Cat. #P4864
Ribonuclease A	Sigma-Aldrich	Cat. #R6513
Torin1	Sigma-Aldrich	Cat. #475991
Rapamycin	Sigma-Aldrich	Cat. #R8781
Chloroquine diphosphate salt	Sigma-Aldrich	Cat. #C6628
Bafilomycin A1 from Streptomyces griseus	Sigma-Aldrich	Cat. #B1793
AOA	Sigma-Aldrich	Cat. #C13408
R162	Calbiochem	Cat. #5.38098
Tamoxifen	Sigma-Aldrich	Cat. #T5648
(Z)-4-Hydroxytamoxifen	Sigma-Aldrich	Cat. #H7904
Puromycin	Sigma-Aldrich	Cat. #P8833
M199 medium	Thermo Fisher Scientific	Cat. #11150059
Endothelial Cell Growth Medium 2	PromoCell	Cat. #C22011
M199 medium without L-glutamine	Sigma-Aldrich	Cat. #M3769
Heparin	Sigma-Aldrich	Cat. #H4784
Bovine Brain Extract	Lonza	Cat. #CC-4098
L-Glutamine	Thermo Fisher Scientific	Cat. #25030024
L-Glutamine ($^{13}C_5$,9%)	Cambridge Isotope Laboratories, Inc.	Cat. #CLM-1822-H
L-Asparagine	Sigma-Aldrich	Cat. #A0884

Continued

Reagent or resource	Source	Identifier
L-Aspartic acid	Sigma-Aldrich	Cat. # A6558
L-Glutamic acid	Carlo Erba	Cat. # 406484
Dimethyl 2-oxoglutarate	Sigma-Aldrich	Cat. #349631
DAPI (4′,6-Diamidino-2-Phenylindole, Dihydrochloride)	Thermo Fisher Scientific	Cat. #D1306
Goat serum	Merck Millipore	Cat. #S26
Dialyzed Fetal Bovine Serum	Thermo Fisher Scientific	Cat. #26400044
Fetal Bovine Serum	Carlo Erba Reagents	Cat. #FA30WS1810500
SYBR QPCR Supermix w/Rox	Thermo Fisher Scientific	Cat. #11744500
TRIzol™ Reagent	Thermo Fisher Scientific	Cat. #15596018
Lipofectamine 2000	Thermo Fisher Scientific	Cat. #12566014
Mouse CD45 microbeads	Miltenyi Biotec	Cat. #130-052-301
Mouse CD31 microbeads	Miltenyi Biotec	Cat. #130-097-418
Isolectin GS-IB4 From Griffonia simplicifolia, Alexa Fluor™ 488 Conjugate	Thermo Fisher Scientific	Cat. #I21411
Collagenase A	Sigma-Aldrich	Cat. #11088793001
Dynabeads™ Sheep Anti-Rat IgG	Thermo Fisher Scientific	Cat. #11035
Immobilon Forte Western HRP substrate	Millipore	Cat. #WBLUF0500
Gateway® BP Clonase® II	Invitrogen	Cat. #11789100
Gateway™ LR Clonase™ II	Invitrogen	Cat. #11791020
Critical commercial assays		
Cell Fractionation Kit	Abcam	Cat. #ab109719
Lenti-X™ p24 Rapid Titer Kit	Takara Bio USA, Inc.	Cat. #632200
High Capacity cDNA Reverse Transcription Kit	Thermo Fisher Scientific	Cat. #4368814
Pierce™ BCA Protein Assay Kit	Thermo Fisher Scientific	Cat. #23225
Tumor Dissociation Kit	Miltenyi Biotec	Cat. #130-096-730
EZ-Link™ Sulfo-NHS-SS-Biotin	Thermo Fisher Scientific	Cat. #21331
N-GARDE Mycoplasma PCR Reagent set PCR kit	Euroclone	Cat. #EMK090020
Deposited data		
Glutamine metabolism via transamination regulates VEGFR2 translation during angiogenesis	This paper	PRIDE: PXD022379
Experimental models: Cell lines		
Human: HUVEC	Lonza	Cat. #00191027
Human: HEK293T	ATCC	CRL-11268
Mouse: LLC1	ATCC	CRL-1642
Mouse: B16F10	ATCC	CRL-6475
Human breast tumor endothelial cells (BTEC)	(Grange et al., 2006)	University of Turin, Italy
Experimental models: Organisms/strains		
Mouse: Gls$^{tm2.1Sray}$	The Jackson Laboratory	JAX: 017894 Maine, USA
Mouse:Tg:VE-cadherin-(PAC)CreERT2	(Monvoisin et al., 2006)	N/A
Mouse: Tg(Pdgfb-Cre-ERT2)1Frut	(Claxton et al., 2008)	N/A
Mouse: CB17/Icr-*Prkdc^{scid}*/IcrIcoCrl	Charles River	Massachusetts, USA
Mouse: Gls1$^{fl/fl;VE-cadherin-(PAC)Cre-ERT2}$	This paper	N/A
Mouse: Gls1$^{fl/fl;Pdgfb-Cre-ERT2}$	This paper	N/A
Oligonucleotides		
A full list of DNA oligos is presented in Table S3	N/A	N/A

(Continued on next page)

Continued		
Reagent or resource	Source	Identifier
Recombinant DNA		
pRSV-Rev	Addgene	Cat. #12253
pMDLg/pRRE	Addgene	Cat. #12251
pMD2.G	Addgene	Cat. #12259
pLKO.1 shSCR	Addgene	Cat. #17920
pLKO.1 puro	Addgene	Cat. #8453
pLenti CMV Neo DEST	Addgene	Cat. #17392
pDONR TM221	Thermo Fisher Scientific	Cat. #17392
pCDNA3.1-hVEGFR2	Lena Claesson-Welsh's Lab	Uppsala University, Sweden
pLVX-TETONE-GFP-RagC-Q120L	(Napolitano et al., 2020)	University of Naples "Federico II", Italy
Software and algorithms		
GraphPad Prism 8.0	GraphPad	www.graphpad.com
ImageJ	(Gallo-Oller et al., 2018)	https://imagej.nih.gov/ij/
AngioTool software	(Zudaire et al., 2011)	N/A
Bio-Rad CFX Manager™ software version 3.1	Bio-Rad	www.bio-rad.com
Leica software	Leica Application Suite X (LAS X)	https://www.leica-microsystems.com/
ModFit LT™ software	ModFit LT™ software	N/A

RESOURCE AVAILABILITY

Lead contact
Further information and requests for resources and reagents should be directed to and will be fulfilled by the lead contact, Massimo M. Santoro (massimo.santoro@unipd.it).

Materials availability
All unique materials and reagents generated in this study are available from the lead contact upon request.

Data and code availability
- Proteomic data has been deposited to the Proteome Xchange Consortium via the PRIDE partner repository with the dataset identifier PXD022379.
- This paper does not report original code.
- Any additional information required to reanalyze the data reported in this paper is available from the lead contact upon request.

EXPERIMENTAL MODEL AND SUBJECT DETAILS

Cell culture
Human umbilical vein endothelial cells (HUVEC) were purchased from Lonza. HUVEC (EC) below passage 8 were used for experimental manipulations and growth in complete M199: M199 medium supplemented with 20% heat-inactivated fetal bovine serum (FBS), 1mg/mL heparin, 0.2% Bovine Brain Extract, 100U/ml penicillin and 100μg/mL streptomycin. HUVEC were cultured on 0.2% pre-coated gelatin plates. Tumor endothelial cells (TEC) (Bussolati et al., 2003) were cultured in Endothelial Cell Growth Medium 2 (PromoCell) supplemented with 100U/ml penicillin and 100μg/mL streptomycin. HEK293T, LLC, and B16F10 were cultured in DMEM GlutaMax medium containing 10% FBS and 100U/ml penicillin and 100μg/mL streptomycin. All cells were maintained in a 37°C incubator with humidified atmosphere of 5% CO_2 and verified for mycoplasma-free by N-GARDE Mycoplasma PCR Reagent set PCR kit.

Mouse model
Glstm2.1Sray mouse line ($Gls^{fl/fl}$), previously generated by Mingote et al., was purchased from the Jackson Laboratory and bred into the C57Bl/6 mouse background. To obtain inducible EC-specific GLS knockout ($Gls^{i\Delta EC}$) mice, $Gls^{fl/fl}$ mice were cross-bred with tamoxifen (TAM) inducible Tg:$Cdh5$-(PAC)CreERT2 or Tg:($Pdgfb$-CreERT2)[1Frut] mice. Mice were housed under conventional conditions in individual cages in controlled room at 22°C and 12h light/dark cycle with Ad $libitum$ access to food and water and were regularly monitored for weight and food consumption. All experiments conducted on the animals were following the Ethics Committee of the University of Padova and authorized by the Italian Ministry of Health (Permit Numbers: 493/2018-PR and 347/2019-PR).

PCR were performed to detect the floxed and recombined allele (Δ) of GLS in EC isolated form micropulmonary EC as it has been described by Mingote et al. (2015).

METHOD DETAILS

Virus transduction

The specific human shRNAs for GLS, GOT1, and GOT2 were purchased from Sigma (GLS-targeting shRNA TRCN0000051137, GOT1-targeting shRNA TRCN0000034784, GOT2-targeting shRNATRCN0000034827). All sequence used in this study are provide in Table S3. To generate pLenti CMV Neo DEST huVEGFR2 to overexpress human VEGFR2 in EC, first we generated attB-flanked huVEGFR2 from VEGFR2 sequence (GenBank accession number X61656.1) in pcDNA3.1 (received from Lena Claesson-Welsh's Lab). Then, attB-flanked huVEGFR2 was subcloned into pDONR TM 221 using Gateway® BP Clonase® II. Finally, LR recombination reaction was performed with Gateway™ LR Clonase™ II to recombine pDONR TM 221-huVEGFR2 with the destination vector pLenti CMV Neo DEST. Plasmid pLVX-TETONE-GFP-RagC-Q120L received from Andrea Ballabio's Lab. Recombinant lentiviruses carrying shRNA for specific genes, pLVX-TETONE-GFP-RagC-Q120L or pLenti CMV Neo DEST huVEGFR2 were produced by co-transfecting HEK293T cells with a mixture of plasmid DNA from Addgene consisting of pMD2.G (VSV-G envelope), pMDLg/pRRE (Gag/Pol), and pRSV-Rev (Rev) using Lipofectamine 2000 Transfection Reagent according to the manufacturer's recommendations. In parallel, lentiviruses carrying the scramble (shSCR) were produced. Supernatants containing virus were collected, passed through 0.45-μm filters, centrifuge 31,900 rpm (Rotor type 70Ti Beckman) for 2h at 4°C. Pellets were resuspended in 2% BSA in PBS and stored at -80°C. Virus particles were quantified using Lenti-X™ p24 Rapid Titer Kit. EC were infected using 100 MOI, after 24h, the medium was changed, and cells were collected at the indicated time points for analyses.

Cell viability assay

Cell viability experiments were performed using Crystal Violet staining. Briefly, EC were infected for different lentiviruses and at 72h post-infection, infected and uninfected EC were seeded in 96-well plates at a density of 6×10^3 cells per well. Uninfected cells were treated with 200nM of CB839, 20μM R162 or 2mM AOA in complete M199 medium with or without L-glutamine. Next, viability was evaluated at day 1, 2, 3, 4 and 5 post-seeding. At each time point, the medium was removed, two washes with PBS were performed and 0.5% crystal violet solution was added to each well and incubated for 20min at room temperature on a bench rocker with a frequency of 20 oscillations per minute. The plates were washed four times with tap water and dried. Next, 200μL of methanol was added to each well and absorbance was read at 570nm in Infinite 200 PRO Microplate Reader Tecan.

Cytometric analysis of cell cycle

Cell cycle phases were determined at 96h post-infection (GLS^{KD}) and 24h post-CB839 treatment by flow cytometry. EC were harvested using trypsin-EDTA, washed twice in cold PBS and fixed in 70% ethanol overnight at 4°C. Then, EC were centrifuged, washed, and incubated with PBS containing 50μg/ml propidium iodide and 100μg/ml ribonuclease A for 1h at 37°C. Cell suspensions were run in FACSCanto™ II flow cytometer (BD). Data were analyzed using ModFit LT™ software.

Real time q-PCR

RNA isolation was performed using TRIzol™ Reagent (Thermo Fisher Scientific) according to manufacturer's instructions. RNA concentration and purity were determined using NanoDrop spectrophotometer at A260 and A260/280, respectively. 1μg of RNA was reverse transcribed to cDNA using High-Capacity cDNA Reverse Transcription Kit (Thermo Fisher Scientific). After that, quantitative PCR (q-PCR) was carried out in triplicate using Platinum SYBR Green qPCR SuperMix-UDG with ROX (Thermo Fisher Scientific) on CFX Real-Time PCR Detection System (Bio-Rad). mRNA transcript levels were normalized to β-actin. All primers used in q-PCR have efficiency close to 100% and are listed in Table S3. CFX Manager™ Software version 3.1 (Bio-Rad) was used for performing q-PCR data processing.

Western blotting

After cell treatments, EC were rinsed twice in ice-cold PBS and collected from culture plates by scraping. Cells were lysed in ice-cold RIPA cell lysis buffer (20mM Tris-HCl, pH 7.4, 200mM $NaCl_2$, 2% sodium deoxycholate, 0.2% SDS, 2% NP40, 1x halt protease and phosphatase inhibitor cocktail (Complete Mini, Roche)) for 30 min, and soluble lysate fractions were clarified by centrifugation at 20000 x g for 10min at 4°C. Protein concentrations were determined with Pierce™ BCA Protein Assay Kit. Ten micrograms of protein per well were loaded in SDS-PAGE (4-12% pre-cast gels Invitrogen) and transferred to nitrocellulose membrane. After blocking with 5% milk in TBS-T buffer for 1h, the membranes were incubated with the primary antibodies overnight at 4°C in 1% BSA. Following the incubation, all membranes were washed twice in TBS-T buffer prior to incubation with the appropriate horseradish peroxidase (HRP)-conjugated secondary antibodies (IgG) (1:10,000). The bands were visualized using Immobilon Forte Western HRP substrate and acquired using ChemiDoc™ Imaging System. The band intensities were quantified using Image J software (National Institutes of Health Freeware). Antibodies used in this study are listed in the key resources table. Quantifications are shown as mean ± SD of n=3 independent experiments.

Glutamine deprivation and rescue experiments

For glutamine deprivation assays and rescue experiments, EC were seeded in complete medium M199. After 24h, the medium was replaced with complete M199 without glutamine (-Gln) prepared with 20% dialyzed FBS (dFBS) containing 1mg/mL heparin, 0.2% Bovine Brain Extract, 100u/ml penicillin and 100μg/mL streptomycin. For rescue experiments, EC were treated with 2mM of gluta-mate, 1mM dimethyl 2-oxoglutarate (α-KG), 2mM aspartic acid, or 2mM asparagine for 24h in M199 medium prepared with 20% dFBS, 1mg/mL heparin, 0.2% Bovine Brain Extract, 100u/ml penicillin and 100μg/mL streptomycin.

Metabolite's extraction and quantification

Intracellular metabolites were extracted from EC using a previously established method (Vande Voorde et al., 2019). EC (1×10^5) were plated in 6 wells pre-coated with gelatin plates in complete M199 and infected with different shRNA lentiviruses. After 24h, the medium was replaced with complete M199 prepared with 20% dFBS. The following day medium was replaced with freshly complete M199 prepared with 20% dFBS (6mL/well) and uninfected cells were treated with 200nM CB839, 2mM AOA or deprived for glutamine (using M199 without Gln). For $^{13}C_5$-glutamine tracing experiments, cells were incubated in complete M199 medium prepared with 20% dFBS containing 2mM $^{13}C_5$-glutamine. After 24h, monolayers were washed three times with ice-cold PBS, and extracted with a solution of methanol (50%), acetonitrile (30%) and water (20%). At the endpoint of the experiment, additional wells for each condition were used to quantify the number of cells. The number of cells/well was used to normalize the value of peak area obtained for each metabolite. Cell extracts were centrifuged 20000 g for 10min at 4°C and the supernatants were injected in a Thermo Ultimate 3000 HPLC system with a ZIC-pHILIC column and guard column. The compounds were separated and analyzed as described previously (Vande Voorde et al., 2019). The Q-exactive Plus Orbitrap mass spectrometer (Thermo Fisher Scientific, Waltham, MA, USA) was operated in a polarity switching mode (m/z range 75-1000). For each independent experiment at least three wells/condition were analyzed.

Immunofluorescence analyses

Tumor and gastrocnemius muscle cryosections (10μm) were fixed in 4% PFA for 10 min, blocked in PBS containing 5% goat serum, 1% BSA and 0.3M glycine for 1h. Sections were then incubated with anti-CD31 (1:10, Dianova), anti-alpha smooth muscle actin (α-SMA, 1:100) anti-VEGFR2 (1:100), anti-phosphohistone 3 (Ser10) (1:300), anti-cleaved caspase 3 (c-C3) 5A1E (1:200) antibodies during overnight at 4°C. After that, three washes with PBS were performed and sections were incubated with respectively secondary antibodies Alexa Fluor 568 (1:400) and Alexa Fluor 488 (1:400) and DAPI (300nM) for 1h at 37°C. Sections were washed in PBS three times and mounted in Mowiol 4-88. Samples were analyzed using Confocal Leica SP8 DLS Microscopy. For each tumor and gastroc-nemius sample three sections were performed and for each section 3 to 5 fields were analyzed.

Subcellular fractionation experiments

Mitochondrial and cytosolic fractions were obtained using Cell Fractionation Kit (Abcam) according to manufacturer's instructions. The purity of the fractions was assessed by immunoblotting of COX-IV (1:2,000) and vinculin HVIN-1 (1:8,000).

Biotinylation experiments

VEGFR2 surface expression was measured using Pierce™ Cell Surface Protein Isolation Kit according to manufacturer's instruc-tions. Briefly overnight starved cells were incubated with EZ-Link Sulfo-NHS-SS-Biotin (Thermo Fisher) for 15min at 4°C, washed with quenching solution (50mM glycine in PBS) followed by cell lysis with RIPA buffer and processed for NeutrAvidin Agarose pull down. Cell surface biotinylated proteins were visualized by Western blotting using appropriate antibodies.

Allograft experiments

Gls^fl/fl and *Gls*^iΔEC expressing tamoxifen-inducible Cre-recombinase (Cre-ERT2) under the regulation of the vascular endothelial cad-herin promoter (*Cdh5*) (6-8 weeks of age, males, and females) were injected with 1mg TAM (i.p.) for 10 days within the 2-weeks course (5 days of daily injection, followed by 2 days of recovery and then 5 days of daily injection). After the first week of TAM-injection, LLC (3×10^5) or B16F10 (1.25×10^5) cells were subcutaneously injected in necks and diameters of xenografts were measured using the formula: Tumor volume= (length x width^2)/2, where length indicate the largest tumor diameter and width indicate the perpendicular tumor diameter. Twenty-two/four days after tumor cell inoculation, mice were sacrificed and anatomized.

Isolation of mouse tumor EC

The mouse tumor EC (TEC) were isolated from tumors using magnetic cell sorting system (MiltenyiBiotec). First, tumors (∼0.8g) were dissociated using Tumor Dissociation Kit (MiltenyiBiotec) according to manufacturer's instructions. After dissociation, cell debris were discarded through a cell strainer (70μm) and the remaining cells were washed in PEB buffer (PBS pH 7.2, 0.5% BSA and 2mM EDTA) and centrifuged at 300g for 10min.Then, cells were depleted for CD45 cells using CD45 microbeads (MiltenyiBiotec); after that, cells were labelled with EC marker CD31 microbeads (MiltenyiBiotec) and selected through magnetic cell separation (MACS) columns as recommended by manufacture's experimental procedure MiltenyiBiotec.

Cytometric quantification of TEC

To determine the number of EC in LLC-tumors, tumors were dissociated using Tumor Dissociation Kit (MiltenyiBiotec) as described above. Single cells suspensions were counted using microcytometer chamber. A minimum of 6 x 10^5 cells were stained using APC rat anti-mouse CD31 and PE-Cyanine 7 anti-mouse CD45.2 for 15 min at room temperature in dark. Cells were pelleted (200g for 5 min) and washed in PEB buffer. Cells were resuspended in PEB buffer and run by BD FACSAria™ instrument and analyzed using BD FACSDiva software.

Isolation of micropulmonary of EC

The micropulmonary of EC (MPEC) were isolated using magnetic cell sorting from lung of pups at postnatal day 6 (P6). Lungs were removed from each mouse, rinsed in Hanks' balanced salt solution (Thermo Fisher Scientific) and minced into small pieces for digestion with 1mg/mL collagenase A for 20 min at 37°C. The suspension was passed through a mesh (70μm) to remove large tissue fragments to obtain a cellular suspension, centrifuged and resuspended in PEB buffer. Cell suspensions were counted and incubated with rat monoclonal anti-Mouse CD31 (BD Pharmingen™) (10μg of antibody was added per 1 x 10^7 total cells) during 10 min at 4°C. After extensive washing with PEB buffer, cell suspension (0.5 ml) was incubated with the magnetic beads (Dynabeads™ Sheep Anti-Rat IgG, Thermo Fisher Scientific) for 30 min at 4°C with agitation at every 10 min. Bead-bound cells were selected with a magnet, and the supernatant was removed. Three to five washes with PEB buffer were done to remove unbound cells.

Hindlimb ischemia model

Three months old (male and female) Gls^fl/fl^ and Gls^iΔEC^ mice expressing tamoxifen-inducible Cre-recombinase (Cre-ERT2) under the regulation of the vascular endothelial cadherin promoter ($Cdh5$) were treated with 2mg TAM for 5 days (i.p). After that, mice were anaesthetized (zolazepam-tiletamine 40mg/kg and Xylazine 5mg/kg) and body temperature maintained on a circulating heated water pad. Following a 1 cm groin incision, the neurovascular pedicle was visualized a stereomicroscope (ZEISS SteREO Discovery.V8). The femoral nerve and vein were separated from the femoral artery allowing the ligation of femoral artery. Once the artery was occluded, the surgical site was inspected for any residual bleeding. After, 10 days post-femoral artery ligation mice were sacrificed, and gastrocnemius muscles were extracted.

Retinal angiogenesis and quantification

For analysis of angiogenesis in the retina, postnatal female and male mice expressing tamoxifen-inducible Cre-recombinase (Cre-ERT2) under the regulation of the vascular endothelial Platelet-derived growth factor B (PDGFB) promoter were injected intraperitoneally with 25μl of 4-hydroxytamoxifen (4-OH-TAM) (4mg/ml) on postnatal days (P) 1, 2, 3 and retinas were harvested on P7. Control animals were littermates without CreERT2 expression. For rescue experiments, a single dose of 69nL of 20mM aspartate was injected into the vitreous cavity of P5 mice using a Nanoliter 2010 microinjector (World Precision Instruments) of one eye of all mice whereas the vehicle (PBS) into contralateral eye.

To analyze postnatal retina angiogenesis, whole mouse eyes were washed in PBS and fixed in 4% PFA on ice for 5 min. Eyes were washed in PBS, and the retinas were dissected and stored in methanol at -80°C. Retinas were permeabilized in 1% BSA and 0.5% Triton X-100 (in PBS) at 4°C overnight. Retinas were rinsed in PBS, washed twice in PBLEC buffer (0.1mM CaCl$_2$, 0.1mM MgCl$_2$, 0.1mM MnCl$_2$ and 1% Triton X-100 in PBS), and incubated in 20μg/ml isolectin GS-IB4 Alexa Fluor TM 488-conjugate (Thermo Fisher Scientific) for 4h at 4°C. Retinas were washed five times for 20 minutes in PBS and left in PBS at 4°C overnight. After blocking in 2% goat serum, 1% BSA and 0.5% Triton X-100 (in PBS) for 1 h at room temperature, the retinas were incubated at 4°C overnight in blocking buffer containing the p-4EBP1 (1:200, Cat. #. 2855, CST) primary antibody. After five washes with PBS, retinas were incubated with Alexa Fluor 568-conjugated secondary antibodies (1:500) in blocking buffer for 2 h at room temperature. Before flat-mounting for imaging, retinas were washed four times for 20 min in PBS and partially cut into four leaflets. All quantifications were done on high-resolution confocal images. EC area, vessel length and number of branching points were quantified using the Angiotool software, considering vascular fields behind the angiogenic front in a region between an artery and a vein. All parameters were quantified in a minimum of four vascularized fields per sample.

Polysomal profile analysis

EC were lysed in 30 mM Tris-HCl, pH 7.5, 100 mM NaCl, 30 mM MgCl2, 0.1% NP-40, 100μg/ml cycloheximide and 30 U/ml RNasin. Lysates were clarified at 12,000 rpm for 10 min at 4 °C and cytoplasmic extracts with equal amounts of RNA were loaded on a 15-50% sucrose gradient and centrifuged at 4 °C in a SW41Ti Beckman rotor for 3 h 30 min at 39,000 rpm. Absorbance at 254 nm was recorded by BioLogic LP software (BioRad) and fractions (1 ml each) were collected for subsequent RNA extraction. Where indicated, cells were treated with CB839 (200nM), R162 (20μM), AOA (2mM) for 24h Torin1 (100nM) for 1h. For polysome profiling analysis of GOT1^{KD} and SCR were lysed at 96h post-infection. For total, subpolysomal and polysomal RNA extractions from sucrose gradient aliquots, samples were incubated with 100μg/mL proteinase K and 1% SDS for 2 h at 37°C. RNA was then extracted by phenol/chloroform-isoamyl alchool procedure. Reverse transcription was performed using High-Capacity cDNA Reverse Transcription Kit (Thermo Fisher Scientific). Quantitative PCR (q-PCR) was carried out in triplicate with Platinum SYBR Green qPCR SuperMix-UDG with ROX (Thermo Fisher Scientific) on CFX Real-Time PCR Detection System (Bio-Rad).

Proteomic analysis

For proteomic analysis 5 x 10⁵ HUVEC were seeded into a 10 cm cell culture dish in complete medium M199. After 24h, the medium was replaced with complete M199 prepared with 20% dialyzed FBS and cells were treated with 200nM CB839, 2mM AOA or gluta-mine starved during 24h. After that, HUVEC were washed two times with ice-cold PBS and cells were scraped on ice. Proteins were precipitated in acetone and then reduced and alkylated in a solution of 6M Guanidine-HCl, 5mM TCEP, and 55mM chloroacetamide. Peptides were obtained digesting proteins with LysC (WAKO) for 3h at 37°C and with the endopeptidase sequencing-grade Trypsin (Promega) overnight at 37°C. Collected peptide mixtures were concentrated and desalted using the Stop and Go Extraction (STAGE) technique (Rappsilber et al., 2003). Instruments for LC MS/MS analysis consisted of a NanoLC 1200 coupled via a nano-electrospray ionization source to the quadrupole-based Q Exactive HF benchtop mass spectrometer (Michalski et al., 2011). Peptide separation was carried out according to their hydrophobicity on a PicoFrit column, 75mm ID, 8Um tip, 250mm bed packed with Reprosil-PUR, C18-AQ, 1.9mm particle size, 120 Angstrom pore size (New Objective, Inc., cat. PF7508-250H363), using a binary buffer system consisting of solution A: 0.1% formic acid and B: 80% acetonitrile, 0.1% formic acid. Runs of 120 min after loading were used for proteome samples, with a constant flow rate of 300nl/min. After sample loading, run start at 5% buffer B for 5min, followed by a series of linear gradients, from 5% to 30% B in 90min, then a 10 min step to reach 50% and a 5 min step to reach 95%. This last step was maintained for 10 min. Q Exactive HF settings: MS spectra were acquired using 3E6 as an AGC target, a maximal injection time of 20ms and a 120,000 resolution at 200m/z. The mass spectrometer operated in a data dependent Top20 mode with sub sequent acquisition of higher-energy collisional dissociation (HCD) fragmentation MS/MS spectra of the top 20 most intense peaks. Resolution, for MS/MS spectra, was set to 15,000 at 200m/z, AGC target to 1E5, max injection time to 20ms and the isolation window to 1.6Th. The intensity threshold was set at 2.0 E4 and Dynamic exclusion at 30 seconds. All experiments were performed in at least three independent biological replicates in a labeling free setting. Data are presented as mean ± e.v. Statistical analysis of two experimental groups was performed using parametric two-tailed Student's t test. For mass spectrometry, all acquired raw files were processed using MaxQuant (1.6.2.10) and the implemented Andromeda search engine. For protein assignment, spectra were correlated with the UniProt human database (v. 2020) including a list of common contaminants. Searches were performed with tryptic specifications and default settings for mass tolerances for MS and MS/MS spectra. Carbamidomethyl at cysteine residues was set as a fixed modification, while oxidations at methionine, acetylation at the N-terminus were defined as variable modifications. The minimal peptide length was set to seven amino acids, and the false discovery rate for proteins and peptide-spectrum matches to 1%. The match-between-run feature with a time window of 1 min was used. For further analysis, the Perseus software (1.6.2.3) was used and first filtered for contaminants and reverse entries as well as proteins that were only identified by a modified peptide. The LFQ Ratios were logarithm zed, grouped and filtered for min. valid number (min. 3 in at least one group). Missing values have been replaced by random numbers that are drawn from a normal distribution. Two sample t-test was performed using FDR=0.05. Probability values (p) <0.05 were considered statistically significant. To identify significant enriched GO terms, we utilized the Enrich R program considering the KEGG. Data visualization was done in the statistical environment R. Peptides with Log₂ Difference ≥ 1 and FDR<0.05 were considered significantly enriched. The mass spectrometry proteomics data have been deposited to the ProteomeXchange Consortium via the PRIDE partner repository with the dataset identifier PXD022379.

Matrigel plug angiogenesis assay

Human tumor endothelial cells (TEC; Bussolati et al., 2003) were silenced for GLS and GOT1 using shRNAs. After 72 h post-infection cells were selected using 1μg/mL puromycin. For the *in vivo* evaluation of angiogenesis, SCID mice (Charles River, 8 weeks males) were injected with 1 x 10⁶ cells (TEC) within Matrigel (Corning). Briefly, cells were counted, resuspended in 50 μl of DMEM (Euroclone), chilled on ice, added to 350 μl of Matrigel at 4°C, and injected subcutaneously into the right and left flank of SCID mice via a 26-gauge needle and a 1-ml syringe. Each mouse received 1 x 10⁶ CTRL (scrambles shRNA) cells on the right and 1X10⁶ GLS^KD or GOT1^KD cells on the left. After 7 days, mice were sacrificed and plugs removed and fixed in 10% buffered formalin, and finally embedded in paraffin. Sections (3 μm) were cut and stained with a Masson trichrome reaction and were examined under a light microscope system. Images for each plug were taken at 20X magnification, and structures containing red blood cells were counted in the inner portion of the section (Lopatina et al., 2019).

QUANTIFICATION AND STATISTICAL ANALYSIS

Statistical analysis was performed in GraphPad Prism 8.0. The values reported in the figures represent mean ± SD calculated from at least three independent experiments. The exact sample size (n) is shown in the figures. Statistical differences were evaluated by using two-tailed one sample t-test for comparison to point-normalized data and a two-tailed unpaired t-test for comparison of two groups. Analysis of variance (ANOVA) one-way ANOVA with Bonferroni's multiple comparisons and two-way ANOVA were used for comparison of more than two groups. The p-values are indicated in each graph. When it is indicated, statistical significance was assessed at *p<0.05, **p<0.01, ***p<0.001, ****p<0.0001; n.s., not significant.